

Article

A Computational and Spectroscopic Analysis of Solvate Ionic Liquids Containing Anions with Long and Short Perfluorinated Alkyl Chains

Karina Shimizu ¹, Adilson Alves de Freitas ^{1,*}, Jacob T. Allred ² and Christopher M. Burba ^{2,*}

¹ Centro de Química Estrutural, Institute of Molecular Sciences, Instituto Superior Técnico, Universidade de Lisboa, Av. Rovisco Pais, 1049-001 Lisboa, Portugal; karina.shimizu@tecnico.ulisboa.pt

² Department of Natural Sciences, Northeastern State University, 611 N Grand Ave., Tahlequah, OK 74464, USA; allredj@nsuok.edu

* Correspondence: adilsondefreitas@tecnico.ulisboa.pt (A.A.d.F.); burba@nsuok.edu (C.M.B.)

Abstract: Anion-driven, nanoscale polar–apolar structural organization is investigated in a solvate ionic liquid (SIL) setting by comparing sulfonate-based anions with long and short perfluorinated alkyl chains. Representative SILs are created from 1,2-bis(2-methoxyethoxy)ethane (“triglyme” or “G3”), lithium nonafluoro-1-butanefluorobutanesulfonate, and lithium trifluoromethanesulfonate. Molecular dynamics simulations, density functional theory computations, and vibrational spectroscopy provide insight into the overall liquid structure, cation–solvent interactions, and cation–anion association. Significant competition between G3 and anions for cation-binding sites characterizes the G3–LiC₄F₉SO₃ mixtures. Only 50% of coordinating G3 molecules form tetradentate complexes with Li⁺ in [(G3)₁Li][C₄F₉SO₃]. Moreover, the SIL is characterized by extensive amounts of ion pairing. Based on these observations, [(G3)₁Li][C₄F₉SO₃] is classified as a “poor” SIL, similar to the analogous [(G3)₁Li][CF₃SO₃] system. Even though the comparable basicity of the CF₃SO₃[−] and C₄F₉SO₃[−] anions leads to similar SIL classifications, the hydrophobic fluorobutyl groups support extensive apolar domain formation. These apolar moieties permeate throughout [(G3)₁Li][C₄F₉SO₃] and persist even at relatively low dilution ratios of [(G3)₁₀Li][C₄F₉SO₃]. By way of comparison, the CF₃ group is far too short to sustain polar–apolar segregation. This demonstrates how chemically modifying the anions to include hydrophobic groups can impart unique nanoscale organization to a SIL. Moreover, tuning these nano-segregated fluorinated domains could, in principle, control the presence of dimensionally ordered states in these mixtures without changing the coordination of the lithium ions.

Keywords: solvate ionic liquid; molecular dynamics simulations; vibrational spectroscopy; apolar–polar structural heterogeneity; charge organization; vibrational mode assignments



Citation: Shimizu, K.; de Freitas, A.A.; Allred, J.T.; Burba, C.M. A Computational and Spectroscopic Analysis of Solvate Ionic Liquids Containing Anions with Long and Short Perfluorinated Alkyl Chains. *Molecules* **2024**, *29*, 2071. <https://doi.org/10.3390/molecules29092071>

Academic Editor: Enrico Bodo

Received: 3 April 2024

Revised: 22 April 2024

Accepted: 25 April 2024

Published: 30 April 2024



Copyright: © 2024 by the authors. Licensee MDPI, Basel, Switzerland. This article is an open access article distributed under the terms and conditions of the Creative Commons Attribution (CC BY) license (<https://creativecommons.org/licenses/by/4.0/>).

1. Introduction

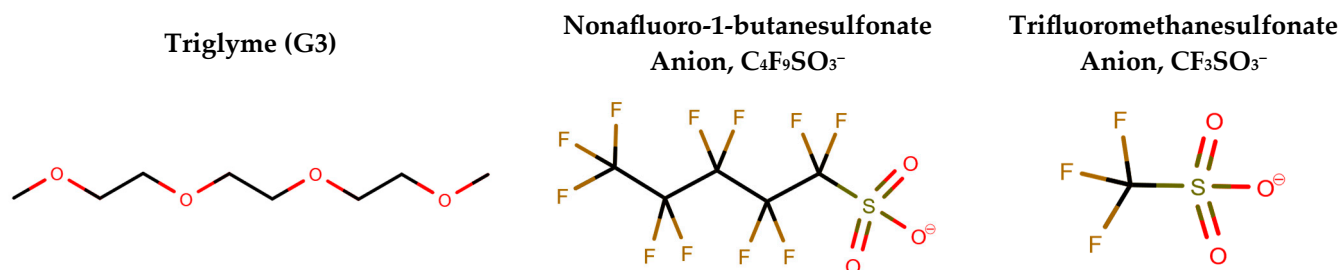
Ionic liquids (ILs) are a class of salts that exist in the liquid phase at or near room temperature. Interest in ILs is motivated, in part, by the unique property combinations available from a completely ionic system. For example, it is relatively easy to make an IL that has high ionic conductivity, a wide electrochemical window, and negligible vapor pressure. However, replicating this set of properties with “traditional” molecular compounds is quite challenging. Tailoring ILs towards specific property combinations requires an understanding of how their liquid-phase structure emerges from long-range Coulombic and short-range repulsive forces [1]. These interactions produce highly interconnected, charge-organized structures with distinct alterations in cation–cation and cation–anion radial distribution functions [2–7]. An additional source of the liquid-phase structure comes from polarity differences within the ions themselves. For example, increasing the length of the aliphatic side chain on 1-alkyl-3-methylimidazolium promotes the self-assembly of the

hydrophobic regions [8–16]. Aggregation of these moieties causes further structural organization of the IL into polar and apolar domains. Similar nanoscale organization may also be driven by the anion when sufficiently long fluorinated alkyl chains are employed [17–20].

ILs are typically classified according to the nature of the constituent ions comprising the material. One early classification scheme divides ILs into protic, aprotic, and zwitterionic groups [21]. However, additional classes have emerged with the advent of new chemical varieties [22]. Solvate ionic liquids (SILs) are an intriguing IL subclass [23–30]. These materials are the product of an inorganic salt and a molecular solvent capable of coordinating the salt's cation. The result is a completely ionic solution that consists solely of complexed cations and dissociated anions. Methyl-capped ethylene glycols, such as triethylene glycol dimethyl ether (triglyme, G3) or tetraethylene glycol dimethyl ether (tetraglyme, G4), are natural choices for the chelating agents due to their high affinity for Li^+ ions. In those cases, polydentate coordination by linear glyme molecules causes the solvent molecule to wrap the cation in a manner that resembles cation coordination by crown ethers [26,29,31–33].

Creating an SIL requires a delicate balance of cation–solvent and cation–anion interactions [24,25]. Strong cation–solvent interactions are needed to eliminate uncoordinated and partially coordinated solvent molecules, while weak ionic interactions are required to minimize cation and anion associations. The relative basicity of the anion compared to the solvent molecule is a key factor in determining the overall SIL liquid structure [26]. For example, the prototypical “good” SIL $[\text{Li}(\text{G4})_1][\text{TFSI}]$, where LiTFSI is lithium bis(trifluoromethanesulfonyl)imide, has few uncoordinated solvent molecules. MD simulations show that approximately 60% of Li-G4 complexes exist in a 1:1 ratio. An additional ~20% of the G4 participates in $[\text{Li}(\text{G4})_2]^+$ or $[\text{Li}_2(\text{G4})]^{2+}$ complexes, with ~15% more G4 forming poly-nuclear $[\text{Li}_x(\text{G4})_y]^{x+}$ complexes with $x + y = 4$. Replacing the weakly coordinating TFSI^- anion with NO_3^- dramatically alters the Li-G4 interactions, increasing the fraction of G4 molecules that lack $\text{Li}\cdots\text{O}$ contacts.

While the influence of anion basicity on the overall liquid structure is well established in SILs, much less is known about how the size of fluorinated alkyl groups attached to the anion drives structural organization in an SIL context. Specifically, how are overall liquid structure, cation–solvent, and cation–anion interactions affected by asymmetrically lengthening a fluorinated alkyl side chain on the anion? We address this question by comparing two SIL systems created from triglyme, lithium trifluoromethanesulfonate (LiCF_3SO_3 , anions with short fluorinated tails), and lithium nonafluoro-1-butanesulfonate ($\text{LiC}_4\text{F}_9\text{SO}_3$, long fluorinated tail). Chemical structures for these species are given in Scheme 1. A combination of MD simulations, density functional theory calculations, and vibrational spectroscopy is employed to understand how the fluorinated side chain length drives SIL structure.



Scheme 1. Structures of the G3 solvent molecule and the two anions that are evaluated. Atom coloring is as follows: fluorine (brown), sulfur (green), and oxygen (red). Carbon and hydrogen atoms are not explicitly shown.

2. Results and Discussion

2.1. Structure of G3–LiC₄F₉SO₃ and G3–LiCF₃SO₃ Mixtures

Figure 1 presents simulation snapshots for different compositions of the [(G3)_nLi][C₄F₉SO₃] mixtures. Hydrophobic interaction among the C₄F₉ groups causes pure LiC₄F₉SO₃ to form distinct polar and nonpolar regions that percolate throughout the simulation box. Strands of Li⁺ ions and SO₃ end groups of the anion generate polar domains with a lamellar structure (Figure S1). The nonpolar subphase is composed of fluoroalkyl moieties. Mixing LiC₄F₉SO₃ with G3 disrupts the mesostructural organization inherent to LiC₄F₉SO₃, leading to a complex liquid phase mediated by cation–solvent, cation–anion, and polar–apolar interactions. The smaller CF₃SO₃[−] anion lacks a large enough fluorinated group to support polar–apolar domain segregation in both high-temperature LiCF₃SO₃ and [(G3)₁Li][CF₃SO₃].

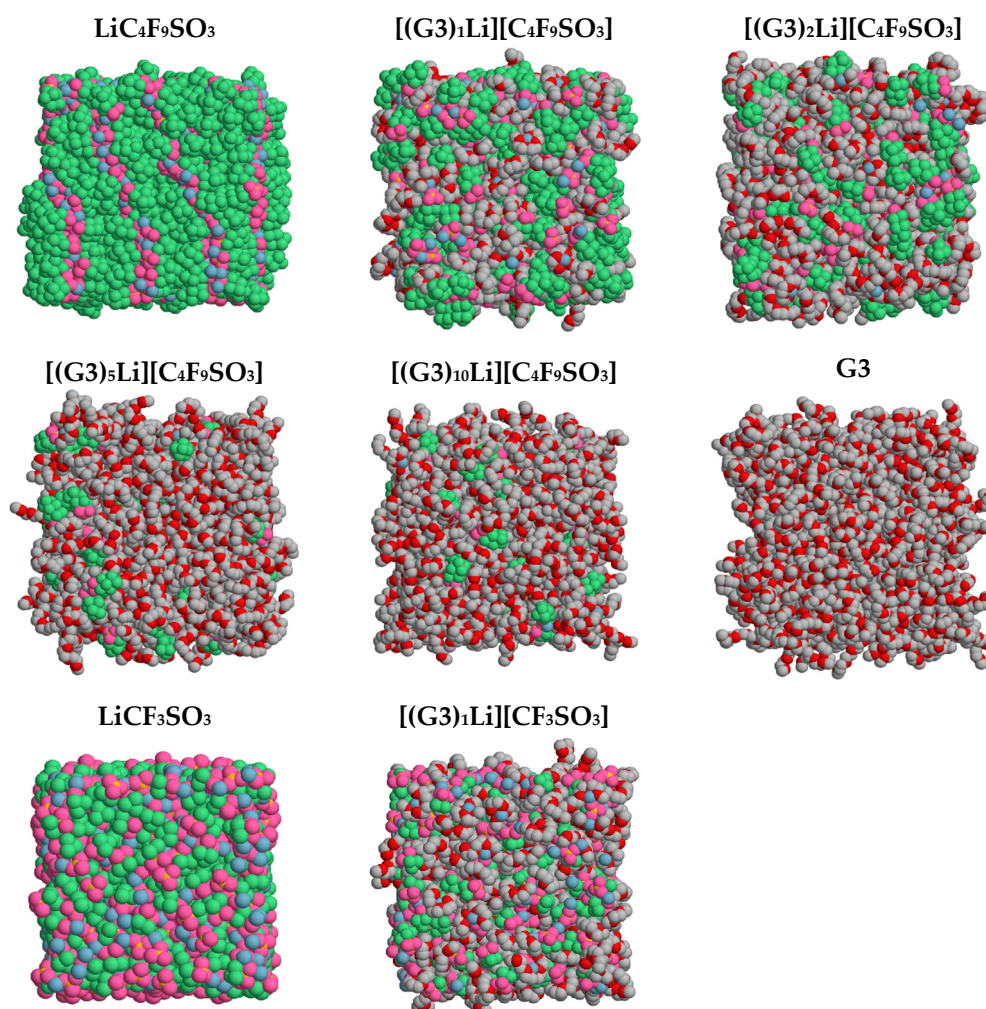


Figure 1. Simulation snapshots of the [(G3)_nLi][C₄F₉SO₃] mixtures with $n = 1, 2, 5,$ and $10,$ [(G3)₁Li][CF₃SO₃], LiCF₃SO₃, LiC₄F₉SO₃, and pure G3. The blue color represents Li⁺ ions; the colors pink, yellow, green, and dark grey denote the O, S, F, and C atoms of the anions, respectively; and the colors red and light grey represent the O and C atoms of the triglyme molecule, accordingly.

Despite their simplicity, radial distribution functions, $g(r)$ s, are a fundamental tool for understanding the local structure of liquids. The $g(r)$ s extracted from the MD trajectories provide the probability of finding a pair of selected sites at a given distance. From their maxima and minima, one can infer preferential atomic positions and define the microstructural pattern of a condensed phase. Furthermore, the Fourier transform of $g(r)$ yields the total scattering functions, which give the X-ray or neutron diffraction profiles when weighted by the appropriate factor. The $g(r)$ s between the Li⁺ ions and O atoms of C₄F₉SO₃[−] and G3

are provided in Figure 2. Both cases show a sharp first peak located at 0.20 nm. Two less intense peaks appear in the $C_4F_9SO_3$ -Li $g(r)$ functions at 0.43 and 0.62 nm. These additional features correspond to the second and third solvation shells centered on the Li^+ ion, respectively. In contrast, the Li-G3 $g(r)$ functions show a featureless second band near 0.65 nm. Integration of $g(r)$ gives the number of neighboring atoms surrounding the central Li^+ ion as a function of distance. These results are presented as dotted lines in Figure 2. Lithium ions are tetrahedrally coordinated by O atoms from the $C_4F_9SO_3^-$ anion in $LiC_4F_9SO_3$ when the coordination shell boundary is placed at ca. 0.30 nm. As the G3 content increases, the integrated $g(r)$ functions reveal a gradual replacement of anions by G3 molecules in the vicinity of the cation. With respect to the fluorobutyl part of the anion, the $g(r)$ functions between the terminal C atoms of the anion produce the peak at 0.49 nm. If the end of the first solvation shell is placed at ca. 0.8 nm, the integrated $g(r)$ function shows a reduction in the number of neighboring anion tails from ~ 10 in the pure salt to ~ 0.50 in $[(G3)_{10}Li][C_4F_9SO_3]$. This emphasizes the overall separation of the anion species as G3 is introduced into the system.

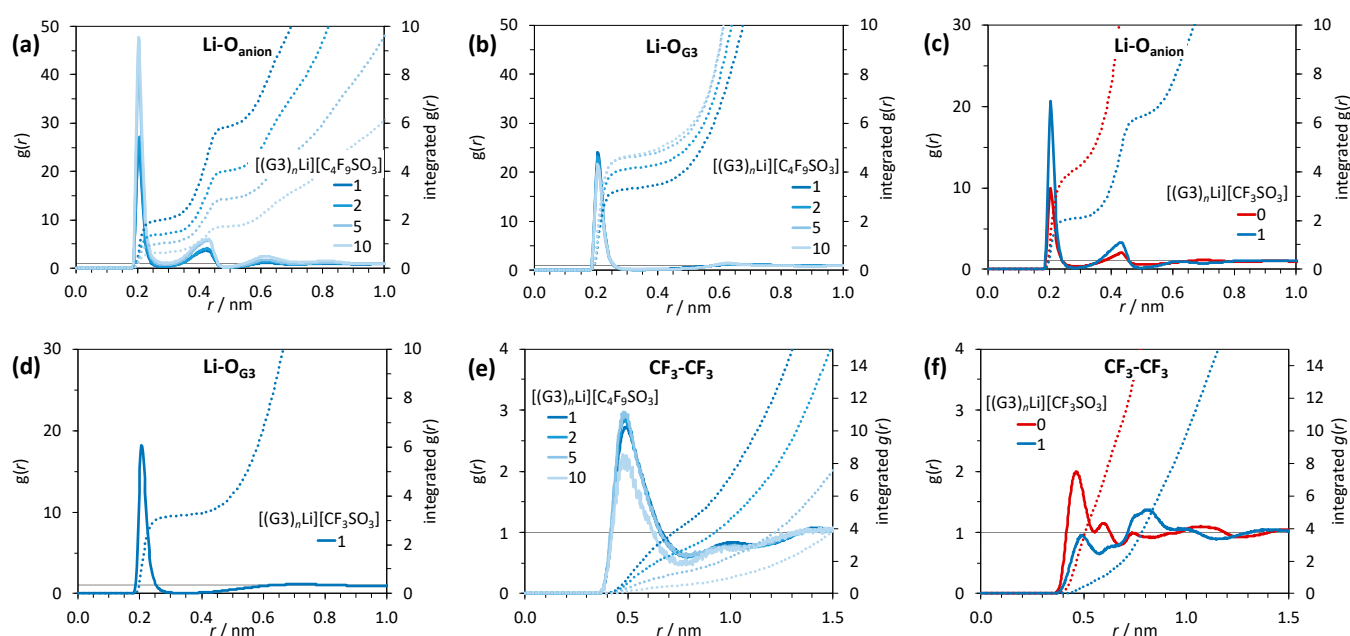


Figure 2. Radial distribution functions, $g(r)$ s, between Li^+ ions and O atoms in $[(G3)_nLi][C_4F_9SO_3]$ and $[(G3)_nLi][CF_3SO_3]$ mixtures, with different compositions. (a,c) O atoms of the sulfonate group, (b,d) O atoms of the ether group, (e) terminal C atoms of the $C_4F_9SO_3^-$ anion, and (f) terminal C atoms of the $CF_3SO_3^-$ anion. The dotted lines represent the integrated $g(r)$.

Radial distribution functions for $[(G3)_1Li][CF_3SO_3]$ are also presented in Figure 2 to explore the role of anion tail size on the liquid structure of these systems. The $g(r)$ profiles for $Li-O_{anion}$ and $Li-O_{G3}$ are quite similar in $[(G3)_1Li][CF_3SO_3]$ and $[(G3)_1Li][C_4F_9SO_3]$. For example, the first sharp peak in the $Li-O_{anion}$ $g(r)$ function is 0.20 nm, and the average coordination number around Li^+ is approximately four. The $g(r)$ data relating distances between the C atoms of the $CF_3SO_3^-$ ion is somewhat different from the $C_4F_9SO_3^-$ anion. The smaller trifluoromethyl group in $CF_3SO_3^-$ causes a displacement in the $g(r)$ maxima from 0.47 to 0.81 nm for $LiCF_3SO_3$ and $[(G3)_1Li][CF_3SO_3]$, respectively. A similar shift is not observed in the corresponding $[(G3)_nLi][C_4F_9SO_3]$ series.

X-ray total structure factors are displayed in Figure 3 for scattering vectors q up to 20 nm^{-1} . Pure $LiC_4F_9SO_3$ exhibits a pre-peak in the low- q region ($2 \leq q/\text{nm}^{-1} \leq 6$), which is a characteristic of segregated polar and apolar domains. This so-called first sharp diffraction peak indicates breaking of the overall charge-ordering homogeneity due to intramolecular polarity differences within the ions. The result is the self-assembly of ions

into mesoscopic structural motifs characterized by complex ionic disorder and charge confinement. By way of comparison, nanoscale structural organization is present for intermediate chain lengths of the 1-alkyl-3-methylimidazolium cation, and cations containing butyl side chains are on the cusp of polar–apolar structural organization [9,11]. The intermediate peak located between 6 and 10 nm^{-1} arises from cation–cation and anion–anion distances within the polar network, while the peak at a larger q value ($10 \leq q/\text{nm}^{-1} \leq 20$) accounts for a multitude of correlations between adjacent atoms (direct contact or adjacency peak). Total structure factor data, $S(q)$, indicate the restoration of the global charge-ordering homogeneity and dilution of the same-charge correlations as the G3 content in the mixture increases. Also, the displacement of the direct contact peak to higher reciprocal distances (i.e., to shorter distances in direct space) is the outcome of the decrease in concentration of the bulky F atoms.

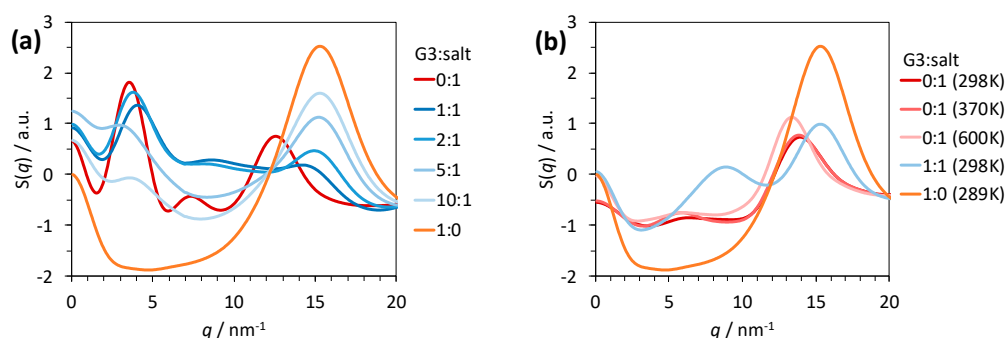


Figure 3. X-ray total structure factors, $S(q)$. (a) $\text{LiC}_4\text{F}_9\text{SO}_3$ at 370 K and $[(\text{G}3)_n\text{Li}][\text{C}_4\text{F}_9\text{SO}_3]$ mixtures with different compositions at 298 K, and (b) LiCF_3SO_3 at different temperatures and the $[(\text{G}3)_1\text{Li}][\text{CF}_3\text{SO}_3]$ mixture at 298 K.

The size of the polar and apolar domains may be determined from probability distribution functions that measure different aggregate sizes; these results are visualized through histograms in Figure 4. Polar domains of the type $\text{Li}^+ - \text{SO}_3^- - \text{Li}^+ - \text{SO}_3^-$ are found in all of the systems; however, the size of these domains depends on the relative amount of G3 and the length of the anion’s fluorinated tail. For instance, the polar domains contain up to 50 units in $[(\text{G}3)_1\text{Li}][\text{C}_4\text{F}_9\text{SO}_3]$, but these domains are broken into smaller-sized aggregates when the G3 content increases to $[(\text{G}3)_{10}\text{Li}][\text{C}_4\text{F}_9\text{SO}_3]$ where the maximum cluster sizes equal four units. Nonpolar domains composed of the fluoroalkyl groups of the anion are also analyzed. The aggregate distributions indicate the presence of small clusters of anions (up to nine units) even in $[(\text{G}3)_{10}\text{Li}][\text{C}_4\text{F}_9\text{SO}_3]$. This underscores the affinity of the fluoro-butyl groups to form supramolecular networks through their hydrophobic interactions.

The CF_3 portion of the CF_3SO_3^- anion is too short to support polar–apolar structural organization, and the $[(\text{G}3)_1\text{Li}][\text{CF}_3\text{SO}_3]$ compound is characterized by a global charge ordering that permeates throughout the bulk phase. This is evident from the absence of a first sharp diffraction peak in the low- q region of the $S(q)$ plots and probability distributions that have nearly all of the LiCF_3SO_3 in the MD simulation box participating in polar domain clusters (up to 300 units). Charge alternation is a feature of room-temperature molten salts. The lack of the charge-ordering peak is most likely a consequence of complete interference cancelation of peaks (same-charge correlations) and anti-peaks (different-charge correlations) [34–36]. Interestingly, the G3 molecule plays a different role in $[(\text{G}3)_1\text{Li}][\text{CF}_3\text{SO}_3]$ compared to $[(\text{G}3)_1\text{Li}][\text{C}_4\text{F}_9\text{SO}_3]$. Adding G3 increases the polar part, which introduces some overall charge ordering and attenuates the charge-ordering peak in $S(q)$ for the $[(\text{G}3)_n\text{Li}][\text{C}_4\text{F}_9\text{SO}_3]$ mixtures. The increase in polar parts of the $[(\text{G}3)_1\text{Li}][\text{CF}_3\text{SO}_3]$ system breaks this global charge ordering, resulting in a more prominent intermediate peak in the 1:1 mixture.

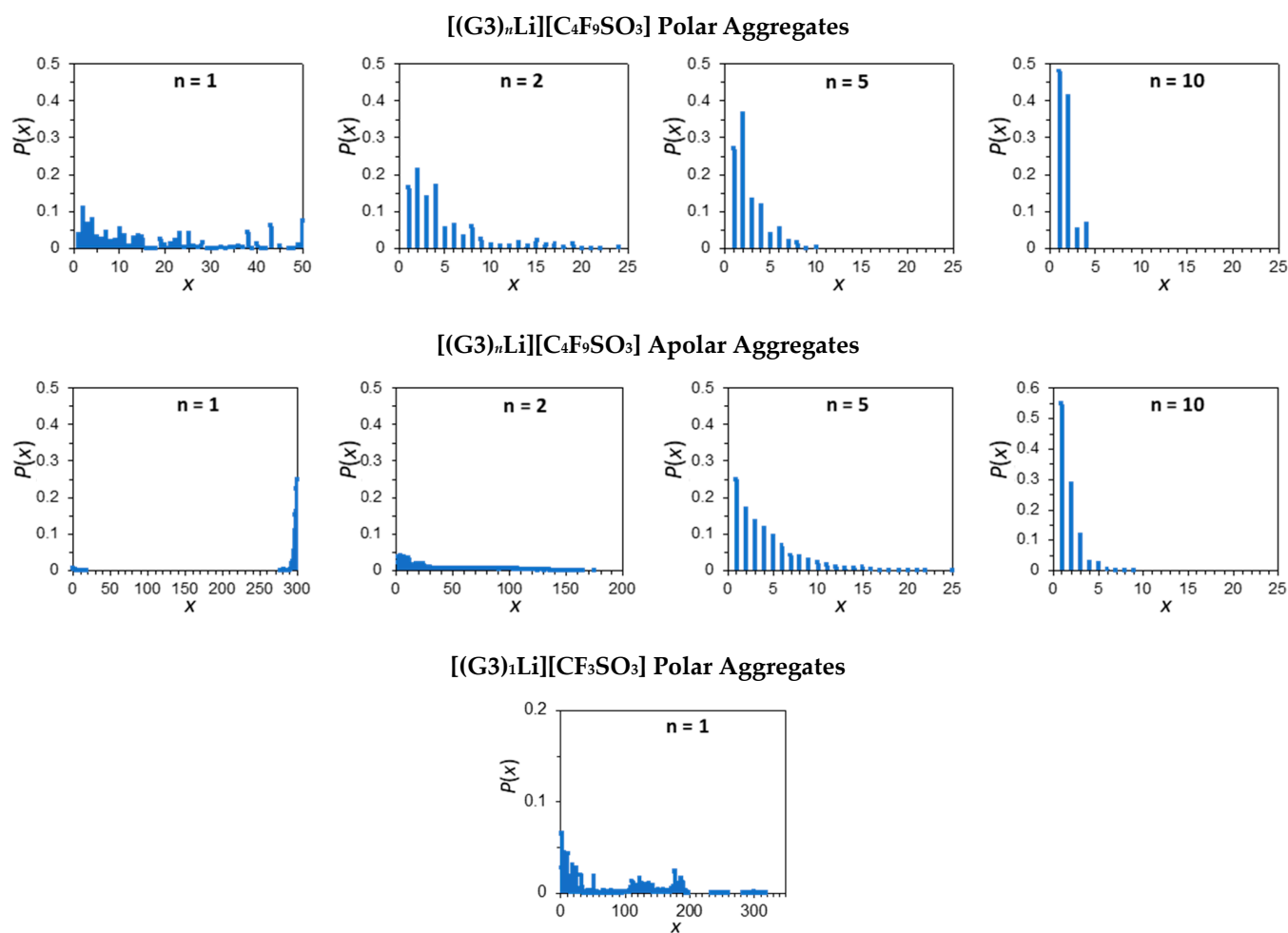


Figure 4. Probability distribution functions $P(x)$ of polar and apolar aggregates involving Li^+ ions and the SO_3^- portion of the anion in $[(\text{G}3)_n\text{Li}][\text{C}_4\text{F}_9\text{SO}_3]$ and $[(\text{G}3)_1\text{Li}][\text{CF}_3\text{SO}_3]$ mixtures ($n = 10, 5, 2,$ and 1). The LiCF_3SO_3 system does not form apolar domains.

2.2. Coordinative Interactions between G3 and Li^+ Ions

A connectivity analysis for pure $\text{LiC}_4\text{F}_9\text{SO}_3$ and its mixtures with G3 was carried out to clarify the environment around the Li^+ ions. These results are presented in Table 1. The $\text{Li}-\text{O}_i$ parameter indicates the number of O atoms of species i coordinated with the cation, while $\text{Li}-i$ represents the number of those species coordinated to the same Li^+ cation. In the pure salt, the $\text{Li}-\text{O}_{\text{anion}}$ and $\text{Li}-\text{anion}$ data place the average number of anions coordinating a central Li^+ ion at slightly fewer than four, and the anions predominantly interact with Li^+ via a single O atom from each sulfonate group. The slightly larger $\text{Li}-\text{O}_{\text{anion}}$ values in comparison to $\text{Li}-\text{anion}$ point to a small contribution of bidentate binding of the anions to the cation. Monodentate anion coordination prevails in all studied compositions.

There is one G3 molecule in the first solvation shell of Li^+ for mixtures up to $[(\text{G}3)_5\text{Li}][\text{C}_4\text{F}_9\text{SO}_3]$. G3 molecules are relatively bulky, and it is difficult to accommodate a second G3 molecule around the small cation. Moreover, G3 coordination must overcome the Coulombic attraction between ion pairs to break the cation free from the anion. Solvation shells with two G3 molecules are more prevalent in $[(\text{G}3)_{10}\text{Li}][\text{C}_4\text{F}_9\text{SO}_3]$, where the fraction of free anions (and thus solvent-separated ion pairs) reaches 50%. Overall, the same observations for $[(\text{G}3)_n\text{Li}][\text{C}_4\text{F}_9\text{SO}_3]$ mixtures are valid for $[(\text{G}3)_1\text{Li}][\text{CF}_3\text{SO}_3]$. In pure LiCF_3SO_3 , there are four anions coordinated by one O atom to the central cation, with a small contribution of bidentate binding. In the 1:1 mixture, the MD simulations reveal one G3 molecule and two CF_3SO_3^- ions in the first solvation shell of the cations.

Table 1. Average number of Li–O connections per lithium ion in $[(G3)_nLi][C_4F_9SO_3]$. Li–O_{anion} and Li–O_{G3} denote the total number of cation–oxygen contacts between Li⁺ and the anions or G3, respectively. Li-anion and Li–G3 stand for single Li-anion and Li–G3 contacts. Li–O_{total} denotes the total number of cation–oxygen connections per Li⁺ ion. Additionally, the percentages of free $C_4F_9SO_3^-$, $CF_3SO_3^-$, and G3 molecules are given.

| <i>n</i> | $[(G3)_nLi][C_4F_9SO_3]$ | | | | | $[(G3)_nLi][CF_3SO_3]$ | | | |
|-----------------------|--------------------------|--------|--------|--------|--------|------------------------|------|------|--------|
| | 0 | 1 | 2 | 5 | 10 | 0 | 0 | 0 | 1 |
| T/K | 370 | 298.15 | 298.15 | 298.15 | 298.15 | 298.15 | 370 | 600 | 298.15 |
| Li–O _{anion} | 3.75 | 1.93 | 1.35 | 0.98 | 0.60 | 3.73 | 3.68 | 3.21 | 2.02 |
| Li-anion | 3.65 | 1.89 | 1.31 | 0.93 | 0.56 | 3.66 | 3.59 | 3.12 | 2.00 |
| Li–O _{G3} | | 2.98 | 3.79 | 4.21 | 4.66 | | | | 2.98 |
| Li–G3 | | 0.92 | 1.17 | 1.31 | 1.54 | | | | 0.90 |
| Li–O _{total} | 3.75 | 4.92 | 5.14 | 5.19 | 5.26 | 3.66 | 3.68 | 3.21 | 5.00 |
| Free anion | | 4% | 16% | 27% | 50% | | | | 3% |
| Free G3 | | 15% | 42% | 74% | 85% | | | | 14% |

Venn diagrams depicting the connectivity between Li⁺ ions and O atoms of G3 molecules at 298 K are shown in Figure 5. The threshold used to account for the connectivity was the end of the first peak in $g(r)$ Li–O_{G3} (ca. 0.275 nm) [26]. As expected, the total number of G3 molecules that interact with Li⁺ ions and the number of O atoms per G3 molecule bound to those ions are sensitive to sample composition. For example, 15.8% of G3 molecules coordinate Li⁺ in the $[(G3)_{10}Li][C_4F_9SO_3]$ sample, and only 25.3% of those molecules experience tetradentate coordination. The presence of a second G3 molecule around the cation results in a larger tridentate population size. Changing the composition to $[(G3)_5Li][C_4F_9SO_3]$ raises the overall fraction of “interacting” G3 molecules to 26.4% as well as the number of tetradentate interaction motifs to 40.9%. Further increases in LiC₄F₉SO₃:G3 ratios to 1:2 and 1:1 increase the percentage of tetradentate G3 among coordinating G3 molecules to 42.4% and 50.3%, respectively. Shortening the fluorinated tail has a marginal impact on tetradentate G3 population sizes. For instance, tetradentate G3 comprises 51.9% of the coordinating G3 molecules in the $[(G3)_1Li][CF_3SO_3]$ mixture.

MD simulations also reveal an alteration in the G3 conformation upon cation coordination. Figure 6 portrays the numbering sequence adopted for the G3 molecule to aid in the discussion of the molecular conformation. Given the symmetry of the G3 moiety, the equivalent dihedral angles of both halves of the molecule were analyzed together. The averaged distribution analyses of torsion angles are provided in Figures S2 and S3. When referring to dihedral angles, we use the following notation: g^\pm for gauche ($\pm 30^\circ$ to $\pm 90^\circ$) and t for trans (150° to 210°).

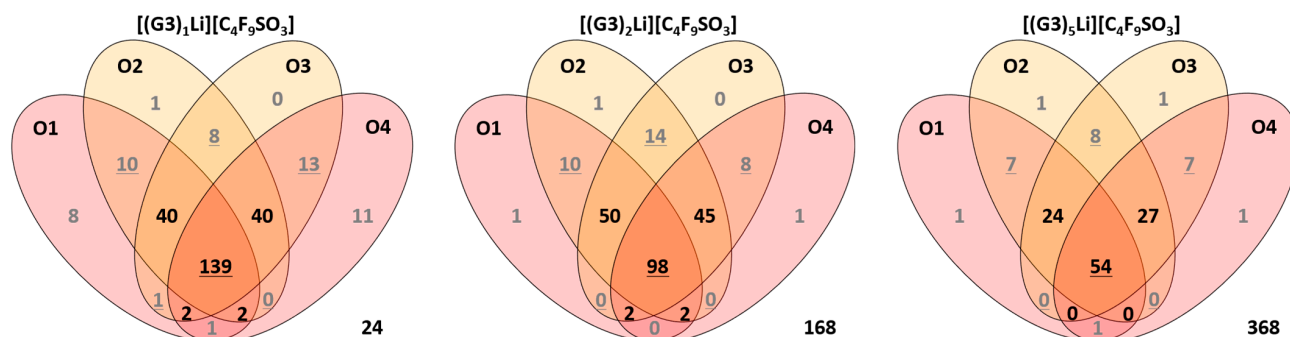


Figure 5. Cont.

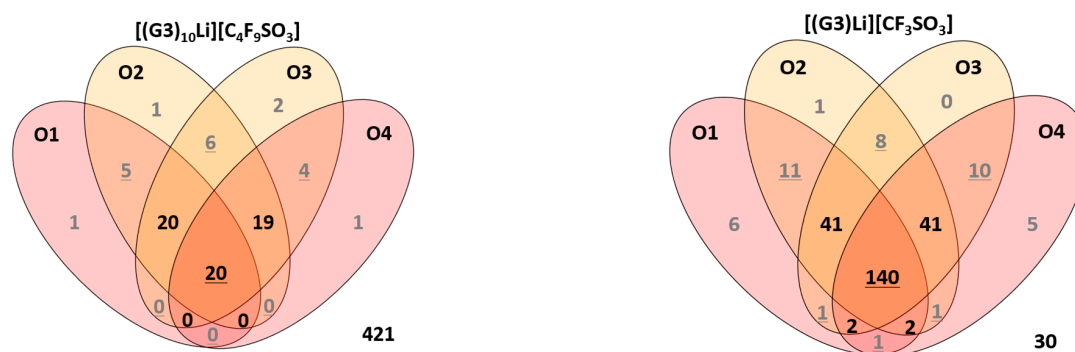


Figure 5. Venn diagrams depicting the connectivity between lithium ions and oxygen atoms of G3 molecules for $[(G3)_nLi][C_4F_9SO_3]$ and $[(G3)_1Li][CF_3SO_3]$ at 298 K. The pink and yellow ellipses correspond to the outermost and inner oxygen atoms of the G3 molecules, respectively. The number of free, noninteracting G3 molecules in each mixture is shown in the bottom right (underlined black numbers = 4 ligating atoms; black numbers = 3 ligating atoms; underlined grey numbers = 2 ligating atoms; grey numbers = 1 ligating atom).

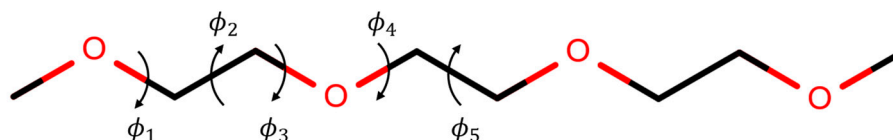


Figure 6. Numbering sequence used in distribution analyses of the G3 molecule's torsion angles (curved arrows).

For the dihedrals of the type COCC, Li–O binding increases the trans population size when moving from pure G3 to $[(G3)_1Li][C_4F_9SO_3]$ (ca. 14% for ϕ_1 and 8% for ϕ_2 and ϕ_3). The OCCO portion of the molecule is predominantly in a gauche conformation for pure G3, and binding with Li^+ further increases the population size of gauche conformers at the expense of the trans conformers. For example, there are reductions of ca. 72% and 87% in trans conformers for ϕ_4 and ϕ_5 , respectively, in $[(G3)_1Li][C_4F_9SO_3]$. Additionally, these dihedrals are displaced to smaller angles.

Complexes between lithium salts and oligomeric ethylene oxides have been extensively studied due to their relevance in lithium battery applications, and it is helpful to compare our MD simulation results with several noteworthy cases. Poly(ethylene oxide) and short-chain ethylene oxide oligomers frequently adopt helical conformations of the $(tgt)_n$ type [37–40]. Lithium ions are six-fold coordinated in the $(G3)_1LiN(SO_2CF_3)_2$ crystal. Each Li^+ is coordinated by the four O atoms of a G3 molecule as well as two O atoms attached to separate S atoms of a single $N(SO_2CF_3)_2^-$ anion [41]. Thus, cations and anions form bidentate contact ion pairs in this solvate structure with the anion arranged in a cisoid conformation. The G3 molecule adopts a $tg^-t.tg^+g^+.tg^+t$ sequence of torsion angles. The $(G3)_1(LiCF_3SO_3)_2$ and $(G3)_1LiN(SO_2C_2F_5)_2$ compounds both exhibit five-fold Li^+ interaction motifs. In $(G3)_1LiN(SO_2C_2F_5)_2$, Li^+ ions interact with all four O atoms of a single G3 molecule plus a single O atom from the anion. This coordination environment produces a $g^-g^-t.tg^+g^+.tg^+t$ torsion angle sequence for G3 [42]. This is contrasted with $(G3)_1(LiCF_3SO_3)_2$, where Li^+ interacts with three O atoms from G3 and two O atoms from separate $CF_3SO_3^-$ anions. The G3 molecule adopts the familiar $tg^+t.tg^-t.tg^+t$ conformation [43]. Similar interaction motifs are found in liquid and polymeric systems [44–46], including $[(G3)_1Li][N(SO_2CF_3)_2]$ and $[(G4)_1Li][N(SO_2CF_3)_2]$ SILs [24,26,33,47].

The cation–solvent interactions predicted by MD simulations may be experimentally verified with vibrational spectroscopy. Infrared and Raman spectra of $[(G3)_nLi][C_4F_9SO_3]$ mixtures are given in Figure 7. A number of the G3 bands experience wavenumber shifts and loss of intensity upon mixing with $LiC_4F_9SO_3$. For example, the 1101 cm^{-1} band, which

contains large amounts of C–O–C stretching motions [40,48–50], red shifts to 1090 cm^{-1} in $[(G3)_1Li][C_4F_9SO_3]$. There are also relatively subtle changes to the CH_2 wagging modes at 1447 and 1472 cm^{-1} as well as decreases in C–H stretching mode intensity. The latter is especially pronounced for the lower-wavenumber C–H bands. The 800 to 900 cm^{-1} region is an especially important spectral region to consider because the bands that occur here are sensitive to the conformation of the ethylene oxide backbone. G3 bands found in this region are mixtures of CH_2 rocking, CO stretching, and CC stretching motions [50]. The characteristic way G3 molecules wrap a Li^+ ion to accommodate tetradentate coordination induces conformational sequences in the backbone that lead to the appearance of a band at 870 cm^{-1} [31,51,52]. It is noteworthy that the 870 cm^{-1} band is present in the crystalline and solution phases of diethylene glycol dimethyl ether (diglyme, G2) and $LiCF_3SO_3$ because it establishes the G3 conformational sequence found in the $(G2)_1LiCF_3SO_3$ crystal is also present in the solution phase [51]. Moreover, the absence of this band in the Raman spectrum of pure G3 has led several groups to use it as a spectroscopic fingerprint for the presence of tetradentate $[(G3)_1Li]^+$ complexes in liquid-phase SILs [24,31,44,46]. Observing the 870 cm^{-1} band in our vibrational spectra is compelling evidence for the presence of these species and confirms the MD simulation results.

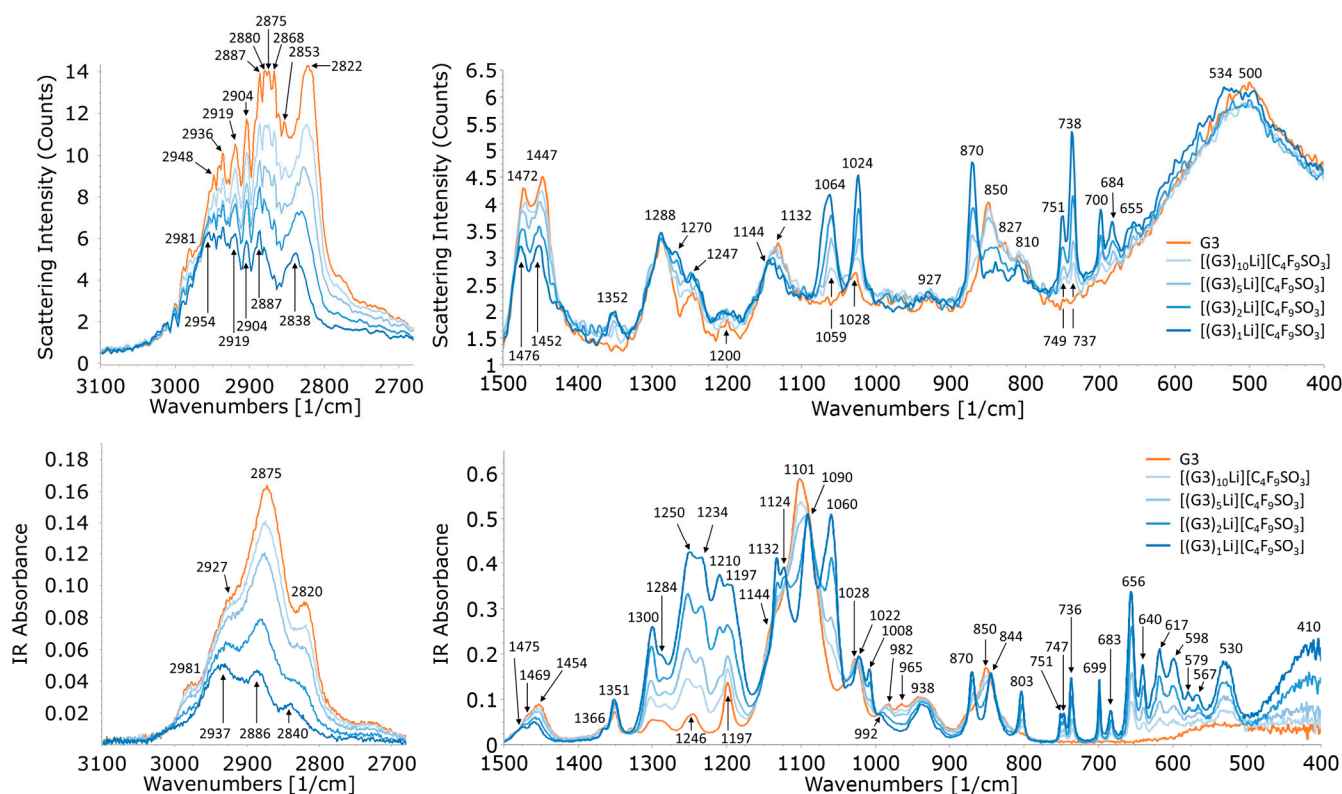


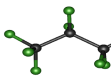
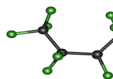
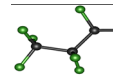
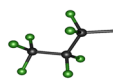
Figure 7. Raman (top) and infrared (bottom) spectra of $[(G3)_nLi][C_4F_9SO_3]$ mixtures.

Additional evidence for Li^+ coordination by G3 molecules and anions is obtained from far-IR spectra of $[(G3)_1Li][C_4F_9SO_3]$ in Figure S4. The SIL exhibits a broad IR band at 414 cm^{-1} that shifts to 438 cm^{-1} upon isotopic substitution with 6Li . This behavior strongly suggests that the band is best assigned as a lithium-ion “cage” mode. These vibrational modes occur when lithium ions undergo translatory motion in a cage-like environment defined by their neighboring atoms. A simplistic model for this mode views the lithium ion as a harmonic oscillator with the ligating O atoms being held stationary. This model predicts an 8% increase in the band wavenumber upon isotopic exchange, which compares quite well with the experimentally observed 6% increase.

2.3. Anion Dihedral Angle Distribution Analysis

Dihedral angle distribution functions for the perfluorobutyl part of the $C_4F_9SO_3^-$ anion are shown in Figure S5. MD simulations reveal a relatively rigid perfluorobutyl chain with SCCC torsion angles adopting a trans conformation. The CCCC torsion angle is slightly skewed from the ideal trans conformation, with a small population of gauche conformers present. The $LiC_4F_9SO_3$ distributions are somewhat different from $[(G3)_nLi][C_4F_9SO_3]$, but this is likely due to the higher temperature used in the simulation of the pure salt. Otherwise, the $LiC_4F_9SO_3:G3$ ratio has a negligible impact on anion conformation. These MD simulation results are augmented by DFT calculations on isolated $C_4F_9SO_3^-$ anions. The stationary-state structures and relative energies of select perfluorobutyl conformations are summarized in Table 2. Consistent with the MD simulations, the tt conformation is the most stable among those investigated. This is followed by slightly less stable tg^\pm and $g^\pm t$ conformers (1–2 kJ mol⁻¹ higher in energy).

Table 2. Relative energies and torsion angles of five $C_4F_9SO_3^-$ conformers.

| Conformation | tt | tg^- | tg^+ | g^+t | g^-t |
|--------------------------|---|---|---|---|---|
| Structure |  |  |  |  |  |
| Relative Energy (kJ/mol) | 0 | 1.79 | 1.82 | 1.52 | 1.54 |
| ∠SCCC | 164.7° | −166.7° | 166.7° | 56.1° | −56.0° |
| ∠CCCC | 162.3° | −54.8° | 54.8° | 162.4° | −162.3° |

Bands associated with the C_4F_9 group are challenging to assign given the potential conformational flexibility. Therefore, a normal coordinate analysis was conducted on these five conformers to aid in the assignments of the anion's vibrational modes. Calculated frequencies, IR intensities, and Raman activities are provided in Table S1; a subset of these results for modes particularly sensitive to the conformation of the C_4F_9 group are collected in Table 3. The majority of the conformationally sensitive anion modes fall between 800 and 680 cm⁻¹. Excellent agreement between experimental and calculated mode frequencies is achieved with the application of a 1.03 scaling factor. The calculations reveal small frequency differences between the g^+ and g^- conformers, making it impossible to distinguish these from one another in the experimental spectra. There is only one possible tt conformation, whereas the gt and tg conformations each have two uniquely different structures that produce the same vibrational spectrum. The expected intensity ratio should be tt:gt:tg = 1:2:2 if all species are present in equal amounts. However, the degeneracy of tg and gt conformers and comparable IR/Raman spectral activities will produce an intensity ratio of 1:4 (tt to the combined sum of gt and tg). The noticeably higher intensities of tt bands relative to the tg or gt bands in the experimental spectra underscore the conclusion that most $C_4F_9SO_3^-$ anions adopt a tt conformation.

Table 3. Assignments for the select vibrational mode of the $C_4F_9SO_3^-$ anion. Scaled frequencies (shown in parentheses) are obtained by multiplying the calculated frequencies by 1.03.

| $[(G3)_1Li][C_4F_9SO_3]$ Frequency/cm ⁻¹ | | $[(G3)_1TBA][C_4F_9SO_3]$ Frequency/cm ⁻¹ | | Calculated $[(G3)_1Li][C_4F_9SO_3]$ Frequencies/cm ⁻¹ | | | | |
|--|-------|---|-------|--|-----------|-----------|-----------|-----------|
| IR | Raman | IR | Raman | tt | tg^- | tg^+ | g^+t | g^-t |
| 683 | 684 | 681 | 682 | | 662 (682) | 662 (682) | 666 (686) | 666 (686) |
| 699 | 700 | 697 | 698 | 681 (702) | | | | |
| 736 | 738 | 734 | 735 | 712 (734) | | | | |
| 747 | | 745 | | | | | 725 (747) | 726 (748) |
| 751 | 751 | 750 | 750 | | 729 (751) | 729 (751) | | |
| 803 | 804 | 800 | 803 | 772 (796) | | | | |

Another perspective on anion structure comes from the disorder longitudinal acoustic mode (D-LAM), which is observed in polymeric and oligomeric C_nH_{n+2} , $C_nH_{n+2}O_n$, and C_nF_{n+2} molecules [52,53]. These modes are characterized by atomic displacements parallel to the skeletal backbone. D-LAMs gain radial atomic motions if the molecule adopts other conformations, which shifts the mode's frequency and broadens the band. Hence, G3's D-LAM serves as an excellent probe of molecular conformation. Calculations put the tt conformer D-LAM at 173 cm^{-1} . The band wavenumber is higher when $C_4F_9SO_3^-$ anion adopts gauche conformations (183 cm^{-1} for tg^\pm , 186 cm^{-1} for g^+t , and 188 cm^{-1} for g^-t conformers). Experimental data place D-LAM at 177 cm^{-1} (Figure S6). This further supports the conclusion that $[(G3)_nLi][C_4F_9SO_3]$ contains a large population of tt anion conformers.

2.4. Ionic Association of Cations and Anions

Competition between G3 molecules and anions for Li^+ is apparent when the lithium complexes are discriminated by ligating molecules in the simulation boxes. The left column of Figure 8 highlights events where Li^+ is complexed simultaneously by anions and G3 molecules. This is contrasted with events where the cations are surrounded only by anions (middle column) and G3 (right column). Even in $[(G3)_{10}Li][C_4F_9SO_3]$, there is at least one anion located inside the solvation shell of about 50% of the Li^+ ions.

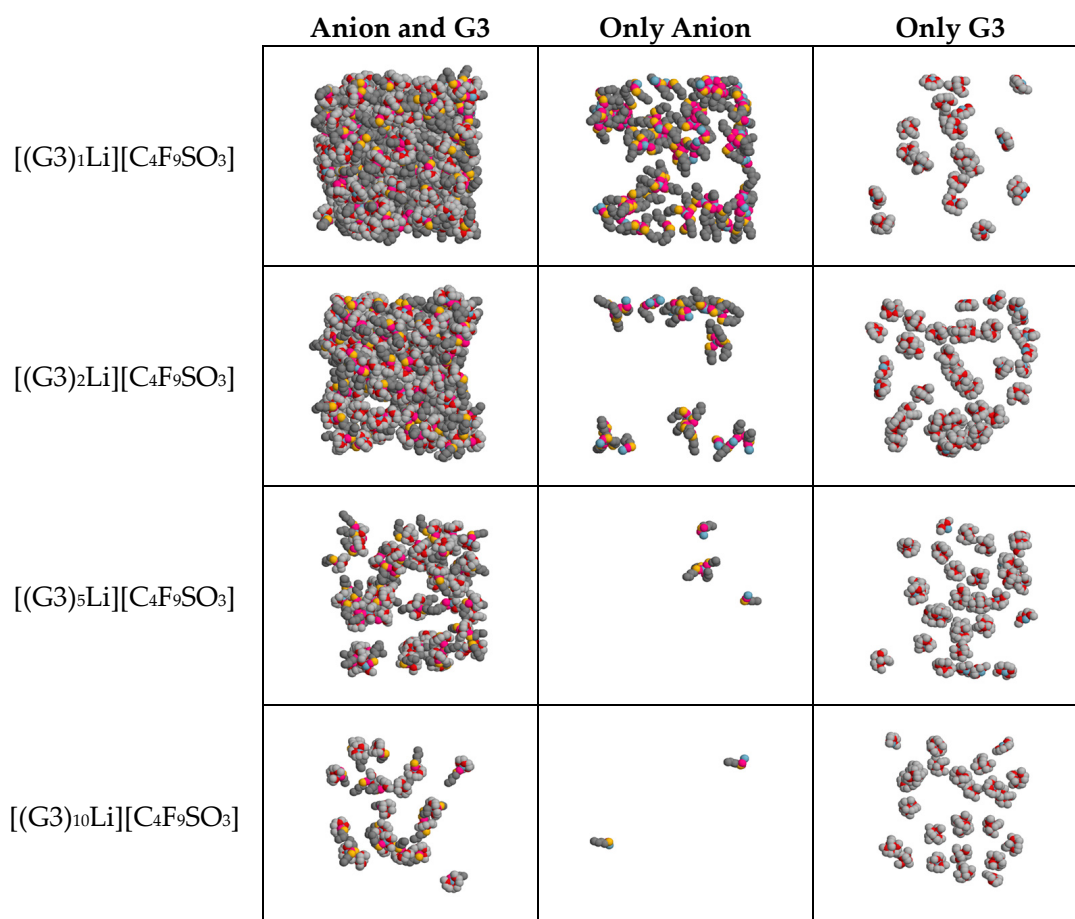


Figure 8. Cont.

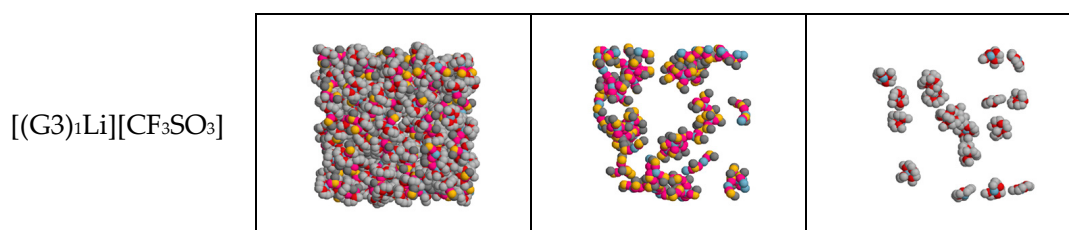


Figure 8. Simulation snapshots of the [(G3)_nLi][C₄F₉SO₃] and [(G3)₁Li][CF₃SO₃] mixtures with different compositions, highlighting the Li⁺ ions coordinated by C₄F₉SO₃[−], CF₃SO₃[−], and G3. The blue color represents Li⁺ ions; the colors pink, yellow, and dark grey denote the O, S, and C atoms of the anion, respectively; the colors red and light grey represent the O and C atoms of the G3 molecule, accordingly.

The ionic association of cations and anions affects the anion's vibrational spectrum in several ways. First, coordination can lower the symmetry of the anion, thereby splitting bands by breaking mode degeneracy. Second, coordination can directly alter the local potential energy environment in which the anion vibrates. Vibrational mode force constants are modulated by the curvature of the corresponding potential energy function; therefore, ionically associated anions may have different band frequencies relative to the uncoordinated "free" anions. Third, ionic association is often accompanied by a redistribution of electric charge throughout a molecule. This affects vibrational mode dipole moment derivatives (IR band intensities) and polarizability derivatives (Raman band intensities).

Prior spectroscopic work on CF₃SO₃[−] suggests that Li⁺ coordination occurs through the SO₃ group [54,55]. Therefore, we begin our analysis with the antisymmetric stretching motions of the S–O bonds $\nu_{as}(\text{SO}_3)$. These bands are presented in Figure 9. [(G3)₁Li][C₄F₉SO₃] contains two $\nu_{as}(\text{SO}_3)$ bands at 1300 and 1250 cm^{−1}. These bands are somewhat closer together in [(G3)₁Li][CF₃SO₃] (43 cm^{−1} separation as opposed to 50 cm^{−1}) and have collapsed into a single asymmetrically broadened band at 1261 cm^{−1} when Li⁺ is exchanged for the charge-protected tetrabutylammonium cation (TBA⁺). Uncoordinated CF₃SO₃[−] ions have C_{3v} symmetry, and the $\nu_{as}(\text{SO}_3)$ modes belong to the doubly degenerate E irreducible representation of this point group. Monodentate or bidentate Li⁺ coordination with the O atoms of CF₃SO₃[−] reduces the symmetry to C_s, causing the $\nu_{as}(\text{SO}_3)$ mode to split into the two observed bands. The C₄F₉SO₃[−] anion's response to coordination—from a spectroscopic point of view—is strikingly similar to CF₃SO₃[−] [54]. This is because both anions experience similar Li⁺⋯O–S-binding motifs. Uncoordinated C₄F₉SO₃[−] anions, however, have only approximate C_{3v} symmetry about the SO₃ portion of the anion. $\nu_{as}(\text{SO}_3)$ degeneracy is not expected for uncoordinated anions. This clarifies why a small amount of splitting is observed in the spectra of [(G3)₁TBA][C₄F₉SO₃] even though direct cation–anion coordination is precluded by the bulky nature of the cation.

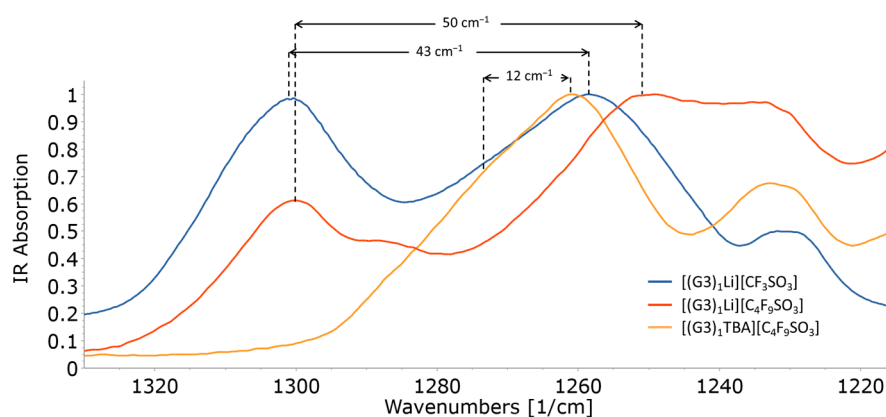


Figure 9. IR spectra of [(G3)₁Li][CF₃SO₃], [(G3)₁TBA][C₄F₉SO₃], and [(G3)₁Li][C₄F₉SO₃].

The amount of $\nu_{\text{as}}(\text{SO}_3)$ splitting might point to slight differences in the strength of the Li-anion coordinative bonds for $[(\text{G}3)_1\text{Li}][\text{C}_4\text{F}_9\text{SO}_3]$ compared to $[(\text{G}3)_1\text{Li}][\text{CF}_3\text{SO}_3]$. The SO_3 symmetric stretching modes $\nu_{\text{s}}(\text{SO}_3)$ give a similar picture as the band is approximately 20 cm^{-1} higher in $[(\text{G}3)_1\text{Li}][\text{C}_4\text{F}_9\text{SO}_3]$ compared to $[(\text{G}3)_1\text{Li}][\text{CF}_3\text{SO}_3]$. A simple Mulliken charge analysis places slightly more negative charge on the O atoms of $\text{C}_4\text{F}_9\text{SO}_3^-$ (average = -0.940 for the tt conformer) compared to CF_3SO_3^- (average = -0.899). This might explain the relative cation–anion interaction strengths.

We now examine anionic interactions from the perspective of the conformationally sensitive bands found in the $800\text{--}680\text{ cm}^{-1}$ region. Figure 10 compares the IR and Raman spectra of $[(\text{G}3)_1\text{Li}][\text{C}_4\text{F}_9\text{SO}_3]$ and $[(\text{G}3)_1\text{TBA}][\text{C}_4\text{F}_9\text{SO}_3]$. Again, the TBAC $_4\text{F}_9\text{SO}_3$ salt proves indispensable for identifying spectroscopic signatures of solvent-separated or otherwise free anions. Replacing Li^+ with TBA^+ causes small ($1\text{--}2\text{ cm}^{-1}$) red shifts in the $\text{C}_4\text{F}_9\text{SO}_3^-$ bands while preserving the relative intensity ratios of the bands. Evidently, ionic association has a marginal effect on the conformational states of the fluorobutyl tails. Normal mode eigenvectors are included in Figure 10 to aid in the interpretation of the frequency shifts. The depicted modes are a mixture of symmetric deformations of the CF_3 group, wagging motions of the CF_2 moieties, and CS stretching. It may seem surprising that these modes are sensitive to cation coordination since the atomic motions involved are far from the SO_3 group. However, this is similar to the LiCF_3SO_3 system where coordination triggers a redistribution of charge throughout the molecule and concomitant stiffening of the $\delta_{\text{s}}(\text{CF}_3)$ force constant [56]. It appears that a similar situation is operative in the related $\text{LiC}_4\text{F}_9\text{SO}_3$ system.

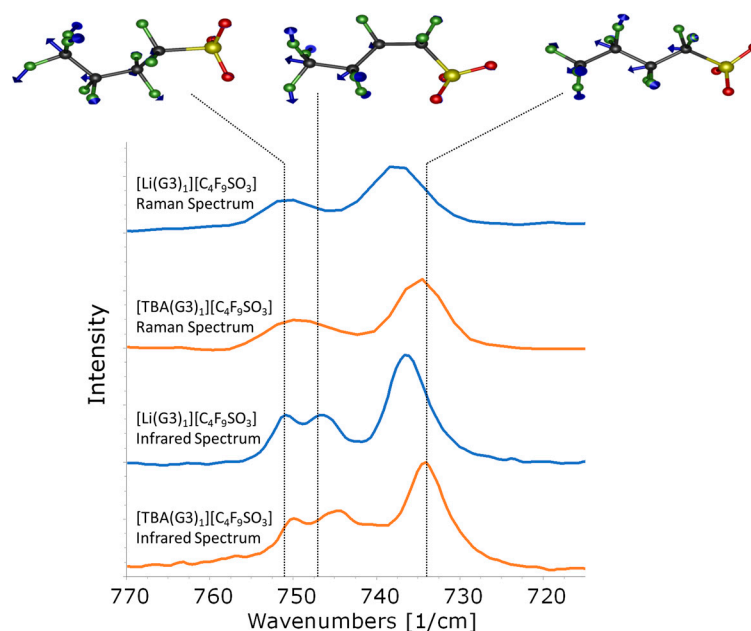


Figure 10. IR and Raman spectra of $[(\text{G}3)_1\text{Li}][\text{C}_4\text{F}_9\text{SO}_3]$ (blue) and $[(\text{G}3)_1\text{TBA}][\text{C}_4\text{F}_9\text{SO}_3]$ (orange). Spectra are displaced along the y-axis for clarity. Normal coordinate eigenvectors are displayed along the top. Vibrational mode amplitudes, which are represented by arrows on the $\text{C}_4\text{F}_9\text{SO}_3^-$ anion, are multiplied by 10 to aid in visualization. The eigenvectors correspond to the following conformers: tg^+ (751 cm^{-1} , left image), g^+t (747 cm^{-1} , middle image), and tt (734 cm^{-1} , right image). Agreement between scaled DFT wavenumber calculations and experimental data is represented by the dotted lines.

Ionically associated anion abundances are composition dependent. The evolution of anion speciation is analyzed through the $\sim 700\text{ cm}^{-1}$ band in Figure 11. This band is selected because it may be assigned solely to tt conformers and is free from band overlap with $\text{G}3$. The band occurs at 698 cm^{-1} and is asymmetrically broadened toward low wavenumbers for $[(\text{G}3)_{10}\text{Li}][\text{C}_4\text{F}_9\text{SO}_3]$, but the band shifts to higher wavenumbers and

gains intensity when additional $\text{LiC}_4\text{F}_9\text{SO}_3$ is added to the mixture. In contrast, the IR spectrum of $[(\text{G3})_1\text{TBA}]\text{C}_4\text{F}_9\text{SO}_3$ contains a single band at 697 cm^{-1} , which is assigned to spectroscopically free anions. Higher-wavenumber bands in $[(\text{G3})_n\text{Li}][\text{C}_4\text{F}_9\text{SO}_3]$ are then assigned to $\text{Li}^+\cdots\text{C}_4\text{F}_9\text{SO}_3^-$ ion pairs.

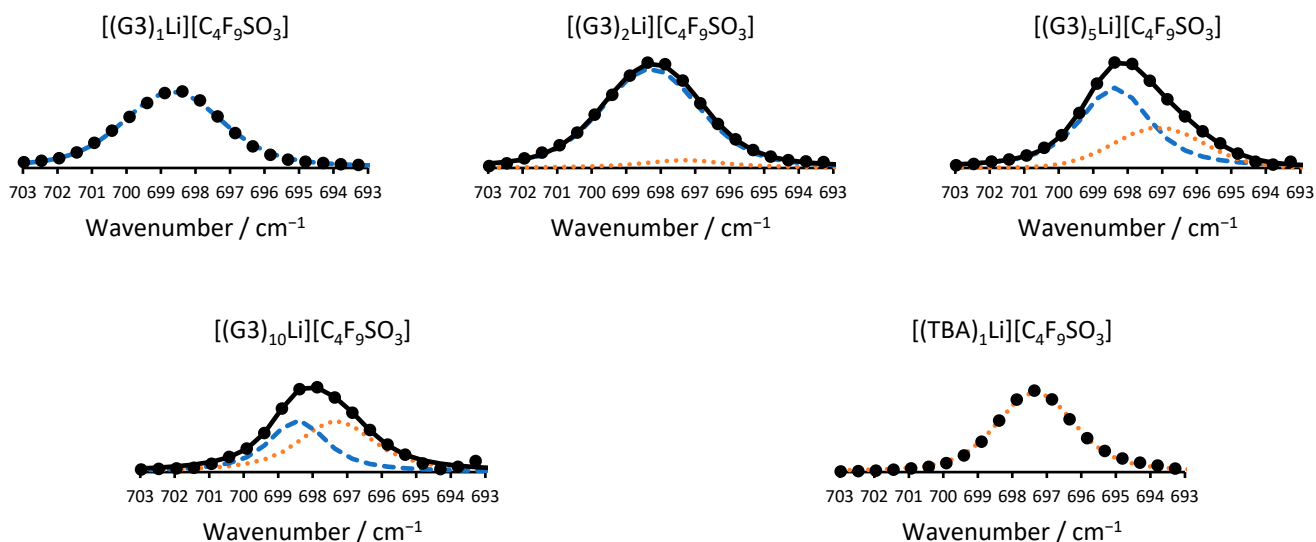


Figure 11. IR spectra of $[(\text{G3})_n\text{Li}][\text{C}_4\text{F}_9\text{SO}_3]$ and $[(\text{G3})_1\text{TBA}][\text{C}_4\text{F}_9\text{SO}_3]$. The blue dashed and orange dotted lines represent ion-paired and free $\text{C}_4\text{F}_9\text{SO}_3^-$ anions, respectively. The sum of the two sub-bands for $n = 2, 5,$ and 10 is shown as a black line. Experimental data are depicted as the black dots.

Quantitative amounts of free and ion-paired anions were determined by fitting the IR spectra of $[(\text{G3})_1\text{TBA}][\text{C}_4\text{F}_9\text{SO}_3]$ and $[(\text{G3})_1\text{Li}][\text{C}_4\text{F}_9\text{SO}_3]$, respectively, with single Voigt functions. Intermediate compositions of $[(\text{G3})_n\text{Li}][\text{C}_4\text{F}_9\text{SO}_3]$ were then modeled with two Voigt functions set at approximately these frequencies. Population sizes of the two species are calculated from the integrated areas of the bands. Results are summarized and compared against the MD simulations in Table 4. Discrepancies between the estimated population sizes are likely due to the effects of charge-scaling and band-fitting procedures. Reduced charges in MD simulations cause ions to be less bound to each other and have higher mobilities. Therefore, one possible explanation is that the scaled charges used in this study lead to underestimated amounts of ion pairs. An additional factor to consider is the difficulty associated with spectral deconvolution when bands are highly overlapped. The band centers differ by only $1\text{--}2\text{ cm}^{-1}$, which could lead to higher amounts of experimental uncertainty in the resulting ion pair population sizes. In spite of these issues, the spectroscopic and MD simulations reveal the same basic trends: $\text{C}_4\text{F}_9\text{SO}_3^-$ anions become highly associated when the salt content is high.

Table 4. Relative population sizes of free and ion-paired $\text{C}_4\text{F}_9\text{SO}_3^-$ anions. MD simulation results are given in parentheses next to the spectroscopically determined values.

| Composition | Ion Pairs | Free Anions |
|--|-----------------------|-------------------------|
| $[(\text{G3})_1\text{Li}][\text{C}_4\text{F}_9\text{SO}_3]$ | 100% (96%) | 0% (4%) |
| $[(\text{G3})_2\text{Li}][\text{C}_4\text{F}_9\text{SO}_3]$ | 92% (86%) | 8% (14%) |
| $[(\text{G3})_5\text{Li}][\text{C}_4\text{F}_9\text{SO}_3]$ | 67% (76%) | 33% (24%) |
| $[(\text{G3})_{10}\text{Li}][\text{C}_4\text{F}_9\text{SO}_3]$ | 56% (50%) | 44% (50%) |
| $[(\text{G3})_1\text{TBA}][\text{C}_4\text{F}_9\text{SO}_3]$ | 0% (N/A) ^a | 100% (N/A) ^a |

^a Not applicable.

Ionic association of the CF_3SO_3^- anion is investigated through the symmetric deformation of the CF_3 part of the anion, $\delta_s(\text{CF}_3)$. This particular vibrational mode is quite sensitive

to anionic speciation, which has led to its frequent use in assessing cation–anion assemblages [56,57]. Table 5 contains the curve-fitting results of $\delta_s(\text{CF}_3)$ for $[(\text{G}3)_1\text{Li}][\text{CF}_3\text{SO}_3]$; vibrational spectra are provided in Figures S7 and S8. The vast majority of the anions participate in either LiCF_3SO_3 ion pairs (70%) or $[\text{Li}_2\text{CF}_3\text{SO}_3]^+$ aggregates (28%). Notably, the amount of free CF_3SO_3^- is low in $[(\text{G}3)_1\text{Li}][\text{CF}_3\text{SO}_3]$.

Table 5. Relative population sizes of $[\text{Li}_x(\text{CF}_3\text{SO}_3)_y]^{x-y}$ anions in $[(\text{G}3)_1\text{Li}]\text{CF}_3\text{SO}_3$.

| Assignment | IR Fit Wavenumber/cm ⁻¹ | IR Band Percentage | Raman Fit Wavenumber/cm ⁻¹ | Raman Band Percentage (Raman) |
|--|------------------------------------|--------------------|---------------------------------------|-------------------------------|
| Free CF_3SO_3^- | 753.4 | 4.3% | 753.4 | 4.6% |
| LiCF_3SO_3 Ion Pair | 757.6 | 49.0% | 757.6 | 44.5% |
| $[\text{Li}_2\text{CF}_3\text{SO}_3]^+$ | 762.1 | 41.1% | 762.2 | 50.2% |
| $[\text{Li}_3\text{CF}_3\text{SO}_3]^{2+}$ | 765.9 | 3.0% | 765.9 | 0.0% |

3. Conclusions

The liquid structure of $\text{G}3\text{-LiC}_4\text{F}_9\text{SO}_3$ and $\text{G}3\text{-LiCF}_3\text{SO}_3$ mixtures are evaluated with MD simulations, DFT calculations, and vibrational spectroscopy. The $\text{C}_4\text{F}_9\text{SO}_3^-$ anion effectively competes with G3 molecules to coordinate lithium ions. This causes a proliferation of ionically associated species and a disruption of tetradentate cation coordination by a single G3 molecule. Similar observations were noted in $[(\text{G}3)_1\text{Li}][\text{CF}_3\text{SO}_3]$, leading Mandai and coworkers [24] to classify the mixture as a “poor” SIL. We also classify $[(\text{G}3)_1\text{Li}][\text{C}_4\text{F}_9\text{SO}_3]$ as a poor SIL given the broad similarities in structural profiles between it and $[(\text{G}3)_1\text{Li}][\text{CF}_3\text{SO}_3]$, amounts of $\text{Li}^+ \cdots \text{C}_4\text{F}_9\text{SO}_3^-$ anionic association, and overall cation coordination environments. In spite of these similarities, the hydrophobic fluorobutyl side chains on the $\text{C}_4\text{F}_9\text{SO}_3^-$ anions exert a strong influence over $\text{G}3\text{-LiC}_4\text{F}_9\text{SO}_3$'s liquid structure. Anionic tails readily self-assemble into hydrophobic domains, even in the relatively dilute $[(\text{G}3)_{10}\text{Li}][\text{C}_4\text{F}_9\text{SO}_3]$ mixture. This is in marked contrast to the $[(\text{G}3)_1\text{Li}][\text{CF}_3\text{SO}_3]$ system where the short CF_3 groups are unable to drive hydrophobic structural organization. This observation provides compelling evidence that SIL liquid structure can be manipulated through structural modifications to the anion.

4. Materials and Methods

4.1. Molecular Dynamics Simulations

The molecular dynamics (MD) simulations were carried out with GROMACS 2020 [58–62]. Triglyme (G3) was modeled using the OPLS-AA force field [63], while $\text{LiC}_4\text{F}_9\text{SO}_3$ and LiCF_3SO_3 were defined with the CL&P force field [64–66], which follows the same framework of OPLS. The partial charges of anion species and Li^+ were scaled by 0.8 based on previous studies, which indicated that this procedure was necessary to obtain results close to the experimental data [67,68]. The procedure for the MD simulations involved the following steps. The initial low-density configurations built with the *fftool* and *Packmol* programs [69,70] were subjected to an MD run with 10^5 steps of 2 fs duration in the *NpT* ensemble, using the *v-rescale* thermostat and Berendsen barostat (τ_T and τ_p couplings of 0.5 ps and 4.0 ps, respectively). This initial short stage brought the simulation boxes to a density resembling that of liquids. Then, annealing stages were performed at 600 K (also with a *v-rescale* thermostat and a Berendsen barostat). Afterwards, the systems were equilibrated at the aimed temperatures using the Nosé–Hoover thermostat and the Parrinello–Rahman barostat at $p = 1$ atm (τ_T and τ_p couplings of 0.5 ps and 4.0 ps, respectively). The production stages in the *NpT* ensemble used the velocity Verlet integration algorithm with a 1 fs timestep, a cutoff radius of 16.0 Å, smooth-particle mesh Ewald method with cardinal B-spline interpolation of order five, fast Fourier transforms with a grid spacing of 0.10 (equilibration and production), and accuracy of Ewald sum kept at 5×10^{-6} at the cutoff (equilibration and production). The covalent bonds with hydrogens were constrained with the LINCS algorithm (fourth-order expansion). The production stages

in the NpT ensemble were 15 ns long, with trajectories recorded every 2 fs in the last 10 ns. Specific details of the MD simulation boxes are listed in Table 6.

Table 6. Details of the MD simulation boxes of the $[(G3)_nLi][C_4F_9SO_3]$ and $[(G3)_nLi][CF_3SO_3]$ mixtures, where N is the number of species in the MD box for a given composition, l_{box} is the final box length, T_{MD} is the temperature, and ρ_{calc} is the calculated density.

| System | N_{salt} | N_{G3} | l_{box}/nm | T_{MD}/K | $\rho_{calc}/g \cdot cm^{-3}$ |
|-----------------------------|------------|----------|--------------|------------|-------------------------------|
| $LiC_4F_9SO_3$ | 600 | 0 | 5.368 | 370.00 | 1.768 |
| $[(G3)_1Li][C_4F_9SO_3]$ | 300 | 300 | 5.462 | 298.15 | 1.481 |
| $[(G3)_2Li][C_4F_9SO_3]$ | 200 | 400 | 5.513 | 298.15 | 1.313 |
| $[(G3)_5Li][C_4F_9SO_3]$ | 100 | 500 | 5.572 | 298.15 | 1.149 |
| $[(G3)_{10}Li][C_4F_9SO_3]$ | 50 | 500 | 5.440 | 298.15 | 1.077 |
| G3 | 0 | 600 | 5.640 | 298.15 | 0.990 |
| $LiCF_3SO_3$ | 600 | 0 | 4.191 | 298.15 | 2.112 |
| $LiCF_3SO_3$ | 600 | 0 | 4.224 | 370.00 | 2.063 |
| $LiCF_3SO_3$ | 1300 | 0 | 5.684 | 600.00 | 1.834 |
| $[(G3)_1Li][CF_3SO_3]$ | 300 | 300 | 5.002 | 298.15 | 1.331 |

4.2. Density Functional Theory Calculations

Structural analyses and vibrational mode calculations of the $C_4F_9SO_3^-$ anion were performed with the GAMESS computational package [71]. Only singlet spin states were considered. Calculations were carried out with the B3LYP hybrid functional, which uses Becke's three-parameter hybrid exchange functional [72] and the Lee–Yang–Parr correlation functional [73,74]. Dunning's augmented correlation-consistent basis set (aug-cc-pVDZ) was used [75]. Default Lebedev grid settings were employed in the calculation (96 radial points in the Euler–MacLaurin quadrature and 302 angular points). Pulay's DIIS converger was used to establish a self-consistent field [76,77]. The energy error threshold for initiating DIIS was 0.5 Hartree, and the maximum size of the DIIS linear equations was ten. The Hessian matrix was computed by numerical differentiation of analytically computed first derivatives. No symmetry constraints were applied in the course of the calculations. The lack of imaginary frequencies in the normal coordinate analysis confirmed that the calculated geometries do not occupy saddle points on the potential energy landscape. Vibrational mode eigenvectors were visualized with WebMO [78].

4.3. Sample Synthesis

Lithium trifluoromethanesulfonate (Sigma Aldrich, St. Louis, MO, USA, CAS #33454-82-9, 99.995%), lithium nonafluoro-1-butanefluorobutanesulfonate (TCI Chemicals, Portland, OR, USA, CAS #131654-65-5, >95.0%), tetrabutylammonium nonafluoro-1-butanefluorobutanesulfonate (Sigma Aldrich, CAS #108427-52-7, $\geq 98.0\%$), and 1,2-bis(2-methoxyethoxy)ethane ("triglyme" or "G3", Sigma Aldrich, CAS #112-49-2, 99%) were used as received. Sample manipulation was performed in an argon-filled glove box with <1 ppm H_2O . Stoichiometric ratios of the salts and solvents were obtained from mass measurements and mixed together in glass scintillation vials by magnetic stirring. Gentle heating on a hot plate was occasionally needed to aid the dissolution process.

4.4. Vibrational Spectroscopy

Attenuated total reflectance Fourier-transform infrared (ATR FT-IR) spectroscopy was used to generate mid-IR (4000–400 cm^{-1}) and far-IR (700–100 cm^{-1}) spectra of the compounds. Mid-IR spectra were collected with a Bruker Alpha FT-IR spectrometer, which was equipped with a single-bounce diamond ATR crystal, a deuterated triglycine sulfate (DTGS) detector, and a SiC globar source. Far-IR spectra were measured with a Nicolet 6700 FT-IR spectrometer. This instrument is equipped with a deuterated lanthanum α alanine-doped triglycine sulfate (DLATGS) detector covered with a polyethylene window and an EverGlo IR source. Samples for far-IR analysis were deposited onto a Harrick

DiaMAX diamond ATR accessory. Mid- and far-IR spectra were collected at 1 cm^{-1} resolution. FT-Raman spectroscopy was performed with a Thermo NXR 9610 Raman spectrometer. Each sample was transferred to a quartz NMR tube and sealed inside an argon-filled glove box. The samples were then measured in a 180° backscattering geometry with a 976 nm excitation laser set to 1.0 W. The spectral resolution was 4 cm^{-1} . All of the vibrational spectra were measured at room temperature and ambient pressure. Spectral deconvolution was performed with Fityk (version 1.3.1) [79].

Supplementary Materials: The following supporting information can be downloaded at <https://www.mdpi.com/article/10.3390/molecules29092071/s1>. Figure S1: Simulation snapshots of pure $\text{LiC}_4\text{F}_9\text{SO}_3$; Figure S2: Dihedral angle distribution functions of the G3 molecule in $[(\text{G}3)_n\text{Li}][\text{C}_4\text{F}_9\text{SO}_3]$ mixtures; Figure S3: Dihedral angle distribution functions of the G3 molecule in $[(\text{G}3)_1\text{Li}][\text{CF}_3\text{SO}_3]$; Figure S4: Far-IR spectra of $[(\text{G}3)_1\text{Li}][\text{C}_4\text{F}_9\text{SO}_3]$ and lithium-6-enriched $[(\text{G}3)_1\text{Li}][\text{C}_4\text{F}_9\text{SO}_3]$; Figure S5: Dihedral angle distribution functions of the $\text{C}_4\text{F}_9\text{SO}_3^-$ ion in $[(\text{G}3)_n\text{Li}][\text{C}_4\text{F}_9\text{SO}_3]$ mixtures; Figure S6: Raman spectra of $[(\text{G}3)_1\text{Li}][\text{C}_4\text{F}_9\text{SO}_3]$ and G3; Figure S7: Transmission IR spectrum of $[(\text{G}3)_1\text{Li}][\text{CF}_3\text{SO}_3]$; Figure S8: Raman spectrum of $[(\text{G}3)_1\text{Li}][\text{CF}_3\text{SO}_3]$; and Table S1: Calculated vibrational mode frequencies, IR intensities, and Raman activities.

Author Contributions: Conceptualization, C.M.B. and K.S.; methodology, C.M.B., K.S. and A.A.d.F.; validation, C.M.B., K.S. and A.A.d.F.; formal analysis, C.M.B., K.S. and A.A.d.F.; investigation, C.M.B., J.T.A., K.S. and A.A.d.F.; data curation, C.M.B., J.T.A., K.S. and A.A.d.F.; writing—original draft preparation, C.M.B., K.S. and A.A.d.F.; writing—review and editing, C.M.B.; visualization, C.M.B., K.S. and A.A.d.F.; supervision, C.M.B. and K.S.; project administration, C.M.B. and K.S.; funding acquisition, C.M.B., K.S. and A.A.d.F. All authors have read and agreed to the published version of the manuscript.

Funding: This work was supported by the donors of ACS Petroleum Research Fund under Undergraduate Research Grant 57803-UR10. C.M.B. served as Principal Investigator on ACS PRF #57803-UR10 that provided support for J.T.A. Manuscript preparation was sponsored by the Office of Naval Research and was accomplished under Grant Number W911NF-23-1-0264 to C.M.B. The views and conclusions contained in this document are those of the authors and should not be interpreted as representing the official policies, either expressed or implied, of the Office of Naval Research or the U.S. Government. The U.S. Government is authorized to reproduce and distribute reprints for Government purposes notwithstanding any copyright notation herein. K.S. and A.A.d.F. thank Fundação para a Ciência e Tecnologia, FCT/MCTES (Portugal) for financial support through CEEC contracts (IST-ID/100/2018 to K.S. and IST-ID/93/2018 to A.A.d.F.), and through projects UIDB/00100/2020 (<https://doi.org/10.54499/UIDB/00100/2020>) and LA/P/0056/2020 (<https://doi.org/10.54499/LA/P/0056/2020>).

Institutional Review Board Statement: Not applicable.

Informed Consent Statement: Not applicable.

Data Availability Statement: The data presented in this study are available on request from the corresponding author due to privacy.

Acknowledgments: C.M.B. and J.T.A. thank the Northeastern State University Department of Natural Sciences for research support toward this project.

Conflicts of Interest: The authors declare no conflicts of interest. The funders had no role in the design of the study; in the collection, analysis, or interpretation of data; in the writing of the manuscript; or in the decision to publish the results.

References

1. Hayes, R.; Warr, G.G.; Atkin, R. Structure and Nanostructure in Ionic Liquids. *Chem. Rev.* **2015**, *115*, 6357–6426. [[CrossRef](#)]
2. Hardacre, C.; McMath, S.E.J.; Nieuwenhuyzen, M.; Bowron, D.T.; Soper, A.K. Liquid Structure of 1,3-Dimethylimidazolium Salts. *J. Phys. Condens. Matter* **2003**, *15*, S159–S166. [[CrossRef](#)]
3. Hardacre, C.; Holbrey, J.D.; Mullan, C.L.; Youngs, T.G.A.; Bowron, D.T. Small Angle Neutron Scattering from 1-Alkyl-3-Methylimidazolium Hexafluorophosphate Ionic Liquids ($[\text{C}_n\text{Mim}][\text{PF}_6]$, $n = 4, 6, \text{ and } 8$). *J. Chem. Phys.* **2010**, *133*, 074510. [[CrossRef](#)]

4. Hardacre, C.; Holbrey, J.D.; McMath, S.E.J.; Bowron, D.T.; Soper, A.K. Structure of Molten 1,3-Dimethylimidazolium Chloride Using Neutron Diffraction. *J. Chem. Phys.* **2003**, *118*, 273–278. [[CrossRef](#)]
5. Deetlefs, M.; Hardacre, C.; Nieuwenhuyzen, M.; Padua, A.A.H.; Sheppard, O.; Soper, A.K. Liquid Structure of the Ionic Liquid 1,3-Dimethylimidazolium Bis((Trifluoromethyl)Sulfonyl)amide. *J. Phys. Chem. B* **2006**, *110*, 12055–12061. [[CrossRef](#)]
6. Triolo, A.; Mandanici, A.; Russina, O.; Rodriguez-Mora, V.; Cutroni, M.; Hardacre, C.; Nieuwenhuyzen, M.; Bleif, H.J.; Keller, L.; Ramos, M.A. Thermodynamics, Structure, and Dynamics in Room Temperature Ionic Liquids: The Case of 1-Butyl-3-Methyl Imidazolium Hexafluorophosphate ([Bmim][PF₆]). *J. Phys. Chem. B* **2006**, *110*, 21357–21364. [[CrossRef](#)]
7. Bernardes, C.E.S.; Shimizu, K.; Lobo Ferreira, A.I.M.C.; Santos, L.M.N.B.F.; Canongia Lopes, J.N. Structure and Aggregation in the 1,3-Dialkyl-Imidazolium Bis(Trifluoromethylsulfonyl)Imide Ionic Liquid Family: 2. from Single to Double Long Alkyl Side Chains. *J. Phys. Chem. B* **2014**, *118*, 6885–6895. [[CrossRef](#)] [[PubMed](#)]
8. Triolo, A.; Russina, O.; Fazio, B.; Triolo, R.; Di Cola, E. Morphology of 1-Alkyl-3-Methylimidazolium Hexafluorophosphate Room Temperature Ionic Liquids. *Chem. Phys. Lett.* **2008**, *457*, 362–365. [[CrossRef](#)]
9. Russina, O.; Triolo, A. New Experimental Evidence Supporting the Mesoscopic Segregation Model in Room Temperature Ionic Liquids. *Faraday Discuss.* **2012**, *154*, 97–109. [[CrossRef](#)]
10. Macchiagodena, M.; Gontrani, L.; Ramondo, F.; Triolo, A.; Caminiti, R. Liquid Structure of 1-Alkyl-3-Methylimidazolium-Hexafluorophosphates by Wide Angle X-Ray and Neutron Scattering and Molecular Dynamics. *J. Chem. Phys.* **2011**, *134*, 114521. [[CrossRef](#)]
11. Triolo, A.; Russina, O.; Bleif, H.-J.; Di Cola, E. Nanoscale Segregation in Room Temperature Ionic Liquids. *J. Phys. Chem. B* **2007**, *111*, 4641–4644. [[CrossRef](#)] [[PubMed](#)]
12. Rocha, M.A.A.; Neves, C.M.S.S.; Freire, M.G.; Russina, O.; Triolo, A.; Coutinho, J.A.P.; Santos, L.M.N.B.F. Alkylimidazolium Based Ionic Liquids: Impact of Cation Symmetry on Their Nanoscale Structural Organization. *J. Phys. Chem. B* **2013**, *117*, 10889–10897. [[CrossRef](#)] [[PubMed](#)]
13. Kashyap, H.K.; Hettige, J.J.; Annapureddy, H.V.R.; Margulis, C.J. SAXS Anti-Peaks Reveal the Length-Scales of Dual Positive-Negative and Polar-Apolar Ordering in Room-Temperature Ionic Liquids. *Chem. Commun.* **2012**, *48*, 5103–5105. [[CrossRef](#)]
14. Santos, C.S.; Annapureddy, H.V.R.; Murthy, N.S.; Kashyap, H.K.; Castner, E.W., Jr.; Margulis, C.J. Temperature-Dependent Structure of Methyltributylammonium Bis(Trifluoromethylsulfonyl)Amide: X-ray Scattering and Simulations. *J. Chem. Phys.* **2011**, *134*, 064501. [[CrossRef](#)]
15. Kashyap, H.K.; Santos, C.S.; Annapureddy, H.V.R.; Murthy, N.S.; Margulis, C.J.; Castner, E.W., Jr. Temperature-Dependent Structure of Ionic Liquids: X-ray Scattering and Simulations. *Faraday Discuss.* **2012**, *154*, 133–143. [[CrossRef](#)]
16. Mackoy, T.; Mauro, N.A.; Wheeler, R.A. Temperature Dependence of Static Structure Factor Peak Intensities for a Pyrrolidinium-Based Ionic Liquid. *J. Phys. Chem. B* **2019**, *123*, 1672–1678. [[CrossRef](#)] [[PubMed](#)]
17. Lo Celso, F.; Yoshida, Y.; Castiglione, F.; Ferro, M.; Mele, A.; Jafta, C.J.; Triolo, A.; Russina, O. Direct Experimental Observation of Mesoscopic Fluorous Domains in Fluorinated Room Temperature Ionic Liquids. *Phys. Chem. Chem. Phys.* **2017**, *19*, 13101–13110. [[CrossRef](#)] [[PubMed](#)]
18. Lo Celso, F.; Appetecchi, G.B.; Simonetti, E.; Keiderling, U.; Gontrani, L.; Triolo, A.; Russina, O. Mesoscopic Structural Organization in Fluorinated Pyrrolidinium-Based Room Temperature Ionic Liquids. *J. Mol. Liq.* **2019**, *289*, 111110. [[CrossRef](#)]
19. Lo Celso, F.; Appetecchi, G.B.; Jafta, C.J.; Gontrani, L.; Canongia Lopes, J.N.; Triolo, A.; Russina, O. Nanoscale Organization in the Fluorinated Room Temperature Ionic Liquid: Tetraethyl Ammonium (Trifluoromethanesulfonyl)(Nonfluorobutylsulfonyl)Imide. *J. Chem. Phys.* **2018**, *148*, 193816. [[CrossRef](#)]
20. Zhao, M.; Wu, B.; Lall-Ramnarine, S.I.; Ramdihal, J.D.; Papacostas, K.A.; Fernandez, E.D.; Sumner, R.A.; Margulis, C.J.; Wishart, J.F.; Castner, E.W., Jr. Structural Analysis of Ionic Liquids with Symmetric and Asymmetric Fluorinated Anions. *J. Chem. Phys.* **2019**, *151*, 074504. [[CrossRef](#)]
21. Armand, M.; Endres, F.; MacFarlane, D.R.; Ohno, H.; Scrosati, B. Ionic-Liquid Materials for the Electrochemical Challenges of the Future. *Nat. Mater.* **2009**, *8*, 621–629. [[CrossRef](#)] [[PubMed](#)]
22. Lei, Z.; Chen, B.; Koo, Y.M.; MacFarlane, D.R. Introduction: Ionic Liquids. *Chem. Rev.* **2017**, *117*, 6633–6635. [[CrossRef](#)] [[PubMed](#)]
23. Tamura, T.; Yoshida, K.; Hachida, T.; Tsuchiya, M.; Nakamura, M.; Kazue, Y.; Tachikawa, N.; Dokko, K.; Watanabe, M. Physicochemical Properties of Glyme-Li Salt Complexes as a New Family of Room-Temperature Ionic Liquids. *Chem. Lett.* **2010**, *39*, 753–755. [[CrossRef](#)]
24. Mandai, T.; Yoshida, K.; Ueno, K.; Dokko, K.; Watanabe, M. Criteria for Solvate Ionic Liquids. *Phys. Chem. Chem. Phys.* **2014**, *16*, 8761–8772. [[CrossRef](#)] [[PubMed](#)]
25. Ueno, K.; Yoshida, K.; Tsuchiya, M.; Tachikawa, N.; Dokko, K.; Watanabe, M. Glyme-Lithium Salt Equimolar Molten Mixtures: Concentrated Solutions or Solvate Ionic Liquids? *J. Phys. Chem. B* **2012**, *116*, 11323–11331. [[CrossRef](#)] [[PubMed](#)]
26. Shimizu, K.; Freitas, A.A.; Atkin, R.; Warr, G.G.; FitzGerald, P.A.; Doi, H.; Saito, S.; Ueno, K.; Umehayashi, Y.; Watanabe, M.; et al. Structural and Aggregate Analyses of (Li Salt + Glyme) Mixtures: The Complex Nature of Solvate Ionic Liquids. *Phys. Chem. Chem. Phys.* **2015**, *17*, 22321–22335. [[CrossRef](#)] [[PubMed](#)]
27. Zhang, C.; Ueno, K.; Yamazaki, A.; Yoshida, K.; Moon, H.; Mandai, T.; Umehayashi, Y.; Dokko, K.; Watanabe, M. Chelate Effects in Glyme/Lithium Bis(Trifluoromethanesulfonyl)Amide Solvate Ionic Liquids. I. Stability of Solvate Cations and Correlation with Electrolyte Properties. *J. Phys. Chem. B* **2014**, *118*, 5144–5153. [[CrossRef](#)]

28. Mandai, T.; Yoshida, K.; Tsuzuki, S.; Nozawa, R.; Masu, H.; Ueno, K.; Dokko, K.; Watanabe, M. Effect of Ionic Size on Solvate Stability of Glyme-Based Solvate Ionic Liquids. *J. Phys. Chem. B* **2015**, *119*, 1523–1534. [[CrossRef](#)]
29. Ueno, K.; Tataru, R.; Tsuzuki, S.; Saito, S.; Doi, H.; Yoshida, K.; Mandai, T.; Matsugami, M.; Umehayashi, Y.; Dokko, K.; et al. Li⁺ Solvation in Glyme–Li Salt Solvate Ionic Liquids. *Phys. Chem. Chem. Phys.* **2015**, *17*, 8248–8257. [[CrossRef](#)]
30. Angell, C.A.; Ansari, Y.; Zhao, Z. Ionic Liquids: Past, Present and Future. *Faraday Discuss.* **2012**, *154*, 9–27. [[CrossRef](#)]
31. Arai, N.; Watanabe, H.; Nozaki, E.; Seki, S.; Tsuzuki, S.; Ueno, K.; Dokko, K.; Watanabe, M.; Kameda, Y.; Umehayashi, Y. Speciation Analysis and Thermodynamic Criteria of Solvated Ionic Liquids: Ionic Liquids or Superconcentrated Solutions? *J. Phys. Chem. Lett.* **2020**, *11*, 4517–4523. [[CrossRef](#)]
32. Tsuzuki, S.; Shinoda, W.; Matsugami, M.; Umehayashi, Y.; Ueno, K.; Mandai, T.; Seki, S.; Dokko, K.; Watanabe, M. Structures of [Li(Glyme)]⁺ Complexes and Their Interactions with Anions in Equimolar Mixtures of Glymes and Li[TFSA]: Analysis by Molecular Dynamics Simulations. *Phys. Chem. Chem. Phys.* **2015**, *17*, 126–129. [[CrossRef](#)] [[PubMed](#)]
33. Tsuzuki, S.; Shinoda, W.; Seki, S.; Umehayashi, Y.; Yoshida, K.; Dokko, K.; Watanabe, M. Intermolecular Interactions in Li⁺-Glyme and Li⁺-Glyme-TFSA⁻ Complexes: Relationship with Physicochemical Properties of [Li(Glyme)][TFSA] Ionic Liquids. *ChemPhysChem* **2013**, *14*, 1993–2001. [[CrossRef](#)] [[PubMed](#)]
34. Araque, J.C.; Hettige, J.J.; Margulis, C.J. Modern Room Temperature Ionic Liquids, a Simple Guide to Understanding Their Structure and How It May Relate to Dynamics. *J. Phys. Chem. B* **2015**, *119*, 12727–12740. [[CrossRef](#)]
35. McDaniel, J.G.; Yethiraj, A. Understanding the Properties of Ionic Liquids: Electrostatics, Structure Factors, and Their Sum Rules. *J. Phys. Chem. B* **2019**, *123*, 3499–3512. [[CrossRef](#)]
36. Sharma, S.; Ivanov, A.S.; Margulis, C.J. A Brief Guide to the Structure of High-Temperature Molten Salts and Key Aspects Making Them Different from Their Low-Temperature Relatives, the Ionic Liquids. *J. Phys. Chem. B* **2021**, *125*, 6359–6372. [[CrossRef](#)]
37. Yokoyama, Y.; Uekusa, H.; Ohashi, Y. Crystal and Molecular Structure of 1,2-Dimethoxyethane Crystallized on a New Diffractometer. *Chem. Lett.* **1996**, *25*, 443–444. [[CrossRef](#)]
38. Matsuura, H.; Miyazawa, T.; Machida, K. Infrared Spectra of Poly(Ethylene Glycol) Dimethyl Ethers in the Crystalline State. *Spectrochim. Acta A* **1973**, *29A*, 771–779. [[CrossRef](#)]
39. Matsuura, H.; Fukuhara, K. Vibrational Spectroscopic Studies of Conformation of Poly(Oxyethylene). II. Conformation–Spectrum Correlations. *J. Polym. Sci. B Polym. Phys.* **1986**, *24*, 1383–1400. [[CrossRef](#)]
40. Tadokoro, H.; Chatani, Y.; Yoshihara, T.; Tahara, S.; Murahashi, S. Structural Studies on Polyethers, [-(CH₂)_m-O]_n. II. Molecular Structure of Polyethylene Oxide. *Makromol. Chem.* **1964**, *73*, 109–127. [[CrossRef](#)]
41. Seo, D.M.; Boyle, P.D.; Sommer, R.D.; Daubert, J.S.; Borodin, O.; Henderson, W.A. Solvate Structures and Spectroscopic Characterization of LiTFSI Electrolytes. *J. Phys. Chem. B* **2014**, *118*, 13601–13608. [[CrossRef](#)] [[PubMed](#)]
42. Henderson, W.A.; McKenna, F.; Khan, M.A.; Brooks, N.R.; Young, V.G., Jr.; Frech, R. Glyme-Lithium Bis(Trifluoromethanesulfonyl) Imide and Glyme-Lithium Bis(Perfluoroethanesulfonyl)Imide Phase Behavior and Solvate Structures. *Chem. Mater.* **2005**, *17*, 2284–2289. [[CrossRef](#)]
43. Frech, R.; Rhodes, C.P.; Khan, M. A Comparison of Local Structures in Crystalline P(EO)₃LiCF₃SO₃ and Glyme-LiCF₃SO₃ Systems. *Macromol. Symp.* **2002**, *186*, 41–49. [[CrossRef](#)]
44. Papke, B.L.; Ratner, M.A.; Shriver, D.F. Vibrational Spectroscopy and Structure of Polymer Electrolytes, Poly(Ethylene Oxide) Complexes of Alkali Metal Salts. *J. Phys. Chem. Solids* **1981**, *42*, 493–500. [[CrossRef](#)]
45. Kaulgud, T.V.; Dhupal, N.R.; Gejji, S.P. Electronic Structure and Normal Vibrations of CH₃(OCH₂CH₂)_nOCH₃-M⁺-CF₃SO₃⁻ (n = 2–4, M = Li, Na, and K). *J. Phys. Chem. A* **2006**, *110*, 9231–9239. [[CrossRef](#)] [[PubMed](#)]
46. Hyun, J.; Dong, H.; Rhodes, C.P.; Frech, R.; Wheeler, R.A. Molecular Dynamics Simulations and Spectroscopic Studies of Amorphous Tetraglyme (CH₃O(CH₂CH₂O)₄CH₃) and Tetraglyme:LiCF₃SO₃ Structures. *J. Phys. Chem. B* **2001**, *105*, 3329–3337. [[CrossRef](#)]
47. Saito, S.; Watanabe, H.; Hayashi, Y.; Matsugami, M.; Tsuzuki, S.; Seki, S.; Canongia Lopes, J.N.; Atkin, R.; Ueno, K.; Dokko, K.; et al. Li⁺ Local Structure in Li-Tetraglyme Solvate Ionic Liquid Revealed by Neutron Total Scattering Experiments with the ^{6/7}Li Isotopic Substitution Technique. *J. Phys. Chem. Lett.* **2016**, *7*, 2832–2837. [[CrossRef](#)] [[PubMed](#)]
48. Yoshihara, T.; Tadokoro, H.; Murahashi, S. Normal Vibrations of the Polymer Molecules of Helical Conformation. IV. Polyethylene Oxide and Polyethylene-D₄ Oxide. *J. Chem. Phys.* **1964**, *41*, 2902–2911. [[CrossRef](#)]
49. Matsui, Y.; Kubota, T.; Tadokoro, H.; Yoshihara, T. Raman Spectra of Polyethers. *J. Polym. Sci. A* **1965**, *3*, 2275–2288. [[CrossRef](#)]
50. Machida, K.; Miyazawa, T. Infrared and Raman Spectra of Polyethylene Glycol Dimethylethers in the Liquid State. *Spectrochim. Acta* **1964**, *20*, 1865–1873. [[CrossRef](#)]
51. Rhodes, C.P.; Frech, R. Local Structures in Crystalline and Amorphous Phases of Diglyme-LiCF₃SO₃ and Poly(Ethylene Oxide)-LiCF₃SO₃ Systems: Implications for the Mechanism of Ionic Transport. *Macromolecules* **2001**, *34*, 2660–2666. [[CrossRef](#)]
52. Johansson, P.; Grondin, J.; Lassègues, J.C. Structural and Vibrational Properties of Diglyme and Longer Glymes. *J. Phys. Chem. A* **2010**, *114*, 10700–10705. [[CrossRef](#)]
53. Grondin, J.; Lassègues, J.-C.; Chami, M.; Servant, L.; Talaga, D.; Henderson, W.A. Raman Study of Tetraglyme–LiClO₄ Solvate Structures. *Phys. Chem. Chem. Phys.* **2004**, *6*, 4260–4267. [[CrossRef](#)]
54. Frech, R.; Huang, W. Anion-Solvent and Anion-Cation Interactions in Lithium and Tetrabutylammonium Trifluoromethanesulfonate Solutions. *J. Solut. Chem.* **1994**, *23*, 469–481. [[CrossRef](#)]

55. Bernson, A.; Lindgren, J. OH End-Group Coordination to Cations and Triflate Ions in PPG Systems. *Polymer* **1994**, *35*, 4842–4847. [[CrossRef](#)]
56. Huang, W.; Frech, R.; Wheeler, R.A. Molecular Structures and Normal Vibrations of CF_3SO_3^- and Its Lithium Ion Pairs and Aggregates. *J. Phys. Chem.* **1994**, *98*, 100–110. [[CrossRef](#)]
57. Frech, R.; Huang, W.; Dissanayake, M.A.K.L. Ionic Association of Lithium Triflate in Glymes, Model Solvents, and High Molecular Weight Poly(Ethylene Oxide). *MRS Proc.* **1994**, *369*, 523–534. [[CrossRef](#)]
58. Bekker, H.; Berendsen, H.J.C.; Dijkstra, E.J.; Achterop, S.; Van Drunen, R.; Van der Spoel, D.; Sijbers, A.; Keegstra, H.; Reitsma, B.; Renardus, M.K.R. GROMACS: A Parallel Computer for Molecular Dynamics Simulations. In *Physics Computing '92*; DeGroot, R.A., Nadrchal, J., Eds.; World Scientific Publishing: Singapore, 1993; pp. 252–256.
59. Berendsen, H.J.C.; Van der Spoel, D.; Van Drunen, R. GROMACS: A Message-Passing Parallel Molecular Dynamics Implementation. *Comput. Phys. Commun.* **1995**, *91*, 43–56. [[CrossRef](#)]
60. Van der Spoel, D.; Lindahl, E.; Hess, B.; Groenhof, G.; Mark, A.E.; Berendsen, H.J.C. GROMACS: Fast, Flexible, and Free. *J. Comput. Chem.* **2005**, *26*, 1701–1718. [[CrossRef](#)]
61. Páll, S.; Abraham, M.J.; Kutzner, C.; Hess, B.; Lindahl, E. Tackling Exascale Software Challenges in Molecular Dynamics Simulations with GROMACS. In *Solving Software Challenges for Exascale*; Markidis, S., Laure, E., Eds.; Springer: Cham, Switzerland, 2015; pp. 3–27. [[CrossRef](#)]
62. Abraham, M.J.; Murtola, T.; Schulz, R.; Páll, S.; Smith, J.C.; Hess, B.; Lindahl, E. GROMACS: High Performance Molecular Simulations through Multi-Level Parallelism from Laptops to Supercomputers. *SoftwareX* **2015**, *1–2*, 19–25. [[CrossRef](#)]
63. Jorgensen, W.L.; Maxwell, D.S.; Tirado-Rives, J. Development and Testing of the OPLS All-Atom Force Field on Conformational Energetics and Properties of Organic Liquids. *J. Am. Chem. Soc.* **1996**, *118*, 11225–11236. [[CrossRef](#)]
64. Canongia Lopes, J.N.; Pádua, A.A.H. Molecular Force Field for Ionic Liquids Composed of Triflate or Bistriflylimide Anions. *J. Phys. Chem. B* **2004**, *108*, 16893–16898. [[CrossRef](#)]
65. Canongia Lopes, J.N.; Pádua, A.A.H. CL&P: A Generic and Systematic Force Field for Ionic Liquids Modeling. *Theor. Chem. Acc.* **2012**, *131*, 1129. [[CrossRef](#)]
66. Shimizu, K.; Almantariotis, D.; Costa Gomes, M.F.; Pádua, A.A.H.; Canongia Lopes, J.N. Molecular Force Field for Ionic Liquids V: Hydroxyethylimidazolium, Dimethoxy-2methylimidazolium, and Fluoroalkylimidazolium Cations and Bis(Fluorosulfonyl)Amide, Perfluoroalkanesulfonylamide, and Fluoroalkylfluorophosphate Anions. *J. Phys. Chem. B* **2010**, *114*, 3592–3600. [[CrossRef](#)] [[PubMed](#)]
67. Thum, A.; Heuer, A.; Shimizu, K.; Canongia Lopes, J.N. Solvate Ionic Liquids Based on Lithium Bis(Trifluoromethanesulfonyl)Imide-Glyme Systems: Coordination in MD Simulations with Scaled Charges. *Phys. Chem. Chem. Phys.* **2020**, *22*, 525–535. [[CrossRef](#)] [[PubMed](#)]
68. Shimizu, K.; Watanabe, M.; Canongia Lopes, J.N.; Freitas, A.A. The Heterogeneous Nature of the Lithium-Ion Diffusion in Highly Concentrated Sulfolane-Based Liquid Electrolytes. *J. Mol. Liq.* **2023**, *382*, 121983. [[CrossRef](#)]
69. Padua, A.; Goloviznina, K.; Gong, Z. *Agiliopadua/Eftool: XML Force Field Files (v1.2.1)*; Zenodo: Geneva, Switzerland, 2021.
70. Martínez, L.; Andrade, R.; Birgin, E.G.; Martínez, J.M. PACKMOL: A Package for Building Initial Configurations for Molecular Dynamics Simulations. *J. Comput. Chem.* **2009**, *30*, 2157–2164. [[CrossRef](#)]
71. Schmidt, M.W.; Baldridge, K.K.; Boatz, J.A.; Elbert, S.T.; Gordon, M.S.; Jensen, J.H.; Koseki, S.; Matsunaga, N.; Nguyen, K.A.; Su, S.; et al. General Atomic and Molecular Electronic Structure System. *J. Comput. Chem.* **1993**, *14*, 1347–1363. [[CrossRef](#)]
72. Becke, A.D. Density-Functional Thermochemistry. III. The Role of Exact Exchange. *J. Chem. Phys.* **1993**, *98*, 5648–5652. [[CrossRef](#)]
73. Lee, C.; Yang, W.; Parr, R.G. Development of the Colle-Salvetti Correlation-Energy Formula into a Functional of the Electron Density. *Phys. Rev. B* **1988**, *37*, 785–789. [[CrossRef](#)]
74. Miehlich, B.; Savin, A.; Stoll, H.; Preuss, H. Results Obtained with the Correlation Energy Density Functionals of Becke and Lee, Yang and Parr. *Chem. Phys. Lett.* **1989**, *157*, 200–206. [[CrossRef](#)]
75. Woon, D.E.; Dunning, T.H., Jr. Gaussian Basis Sets for Use in Correlated Molecular Calculations. III. The Atoms Aluminum through Argon. *J. Chem. Phys.* **1993**, *98*, 1358–1371. [[CrossRef](#)]
76. Pulay, P. Convergence Acceleration of Iterative Sequences. The Case of SCF Iteration. *Chem. Phys. Lett.* **1980**, *73*, 393–398. [[CrossRef](#)]
77. Pulay, P. Improved SCF Convergence Acceleration. *J. Comput. Chem.* **1982**, *3*, 556–560. [[CrossRef](#)]
78. Polik, W.F.; Schmidt, J.R. WebMO: Web-Based Computational Chemistry Calculations in Education and Research. *Wiley Interdiscip. Rev. Comput. Mol. Sci.* **2021**, *12*, e1554. [[CrossRef](#)]
79. Wojdyr, M. Fityk: A General-Purpose Peak Fitting Program. *J. Appl. Crystallogr.* **2010**, *43*, 1126–1128. [[CrossRef](#)]

Disclaimer/Publisher's Note: The statements, opinions and data contained in all publications are solely those of the individual author(s) and contributor(s) and not of MDPI and/or the editor(s). MDPI and/or the editor(s) disclaim responsibility for any injury to people or property resulting from any ideas, methods, instructions or products referred to in the content.